Chapter 4 Oxygen Evolution Reaction Study using $MoSe_2$ based Nanomaterials as Electrodes

4.1 Introduction:

The oxygen evolution reaction (OER) is a seemingly simple yet stubbornly sluggish kinetics of electrons and protons that unlock the potential of hydrogen fuel. However, the high overpotentials associated with the OER act as a bottleneck, hindering efficiency and practicality. Traditional OER electrocatalysts, often based on scarce and expensive noble metal oxides (RuO_2, IrO_2, etc.), offer high activity and stability, but their limitations hinder their widespread applications. Their environmental footprint and economic burden necessitate a shift towards earth-abundant alternatives. This is where transition metal dichalcogenides (TMDs) step onto the stage. Their layered structures and diverse properties whispering promises of a more sustainable future. Their abundance and earth-friendliness align perfectly with sustainability goals. Unlike their traditional counterparts, TMDs offer the tantalizing prospect of tunability – their structure and composition can be meticulously crafted, and their active sites meticulously designed to cater to specific performance requirements. This inherent catalytic activity, coupled with their high electrical conductivity, creates a potent combination for facilitating the intricate charge transfer involved in the OER process. Recent research has unveiled the immense potential of TMDs like $MoSe_2$, MoS_2, WS_2, and WSe_2, showcasing promising OER activity and stability. Scientists are delving deeper, unlocking the secrets to further optimization: sculpting TMDs into metal oxide nanoparticles, nanorods, and even intricate heterostructures to maximize surface area and active sites. Strategically introduce foreign metal (doping/decorating) and manipulate defects to fine-tune their electronic properties for enhanced activity. This alliances with other active materials like metal oxides and conducting supports to create synergistic effects. However, long-term stability under harsh operating conditions, precise control over synthesis, the intricate link between structure and performance, and the seamless integration of these optimized TMDs into practical water-splitting devices are hurdles that demand continued research and innovation. Robust encapsulation strategies are being developed to shield TMDs from harsh environments while scalable and cost-effective synthesis methods are being brought to life. Device design and operating parameters are being meticulously optimized, inching closer to a future where TMD-based OER catalysts bridge the gap between potential and reality. In order to get maximum active edge sites for catalytic activity, different morphologies of $MoSe_2$ based nanostructures have been investigated [31, 77, 125, 129, 130].

4.2 Reaction mechanism for OER:

Water splitting reaction is divided into two half-cell reactions: Cathodic half-cell reaction (hydrogen evolution) and anodic half-cell reaction (oxygen evolution) [86]. The water oxidation (OER) follows different reactions steps to liberate oxygen gas in acidic and alkaline medium, as shown in **Figure 4.1 (a, b).**

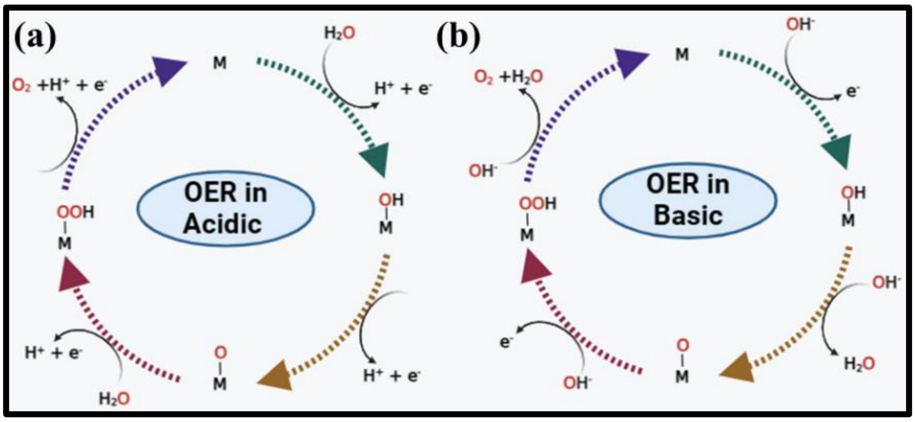

Figure 4.1 *Conventional OER mechanism in (a) acidic and (b) basic medium.*

4.2.1 OER reaction in acidic medium

The OER process in acidic media plays a crucial role in the electrochemical splitting of water and, a method that holds great promise for the sustainable production of hydrogen. Despite its importance, the OER is often seen as a significant hurdle that hampers overall efficiency. This is primarily due to its slow reaction rate and its susceptibility to acidic and oxidative conditions. It's efficiency, determines half-reaction process. In acidic electrolytes, the overall reaction for OER is:

$$2H_2O \rightarrow O_2 + 4H^+ + 4e^- \tag{4.1}$$

The reaction is generally believed to proceed in four following steps:

$$H_2O + * \rightarrow OH^* + H^+ + e^- \tag{4.2}$$

$$OH^* \rightarrow O^* + H^+ + e^- \tag{4.3}$$

$$H_2O + O^* \rightarrow OOH^* + H^+ + e^- \tag{4.4}$$

$$OOH^* \rightarrow * + O_2 + H^+ + e^- \tag{4.5}$$

Here * represents the active site of electrocatalyst.

4.2.2 OER reaction in basic medium

The OER process in basic (alkaline) media is a critical process in various electrochemical systems, including water electrolysis and metal-air batteries. In alkaline electrolytes, the overall reaction for OER is:

$$4OH^- \rightarrow O_2 + H_2O + 4e^- \tag{4.6}$$

The OER process in alkaline medium typically involves the four following steps:[131]

$$* + OH^- \rightarrow OH^* + e^- \tag{4.7}$$

$$OH^* + OH^- \rightarrow O^* + H_2O + e^- \tag{4.8}$$

$$O^* + OH^- \rightarrow OOH^* + e^- \tag{4.9}$$

$$OOH^* + OH^- \rightarrow O_2 + H_2O + e^- + * \tag{4.10}$$

4.3 Performance evolution index for electrocatalyst:

The overall electrode activity, overpotential, the Tafel slope, charge transfer resistance and catalytic durability are important parameters that explain the OER catalytic activity of specific electrocatalyst material.

4.3.1 Overpotential (η)

The overpotential is a common measure used to assess the catalytic activity of an OER electrocatalyst, which exceeds the thermodynamic potential. It propels the reaction at a certain scan rate. The overpotential is the least amount of potential needed to produce oxygen on the surface of the electrocatalyst. The correlation between the overpotential and the overall potential is given by following **equation 4.11**.

$$E_{op} = 1.23 + iR + \eta \tag{4.11}$$

Where E_{op} is the overall potential of electrochemical reactions and iR is the ohmic potential drop due to the resistance of ion flow in the electrolyte. The 1.23 is the reversible thermodynamical potential of water, and η is an overpotential which is estimated by the polarization curve evaluated using linear sweep voltammetry (LSV) measurements.

4.3.2 Tafel slope and exchange current density

Tafel slope indicates the rate-determining step of the reaction. The Tafel slope reflects the intrinsic catalytical activity of a catalyst. The Tafel plot indicates a linear relationship between the applied potential and the logarithmic of current density (log j), as given in equation 3.18 of chapter 3.

4.3.3 Electrochemical impedance spectroscopy (EIS) measurements

EIS serves as a powerful tool for probing the electrochemical behavior of materials or devices. It allows us to extract valuable information about the catalyst's charge transfer resistance and other parameters that are directly linked to the OER activity. This is achieved by applying a minor potential disturbance and observing the subsequent current response. In OER study, the charge transfer resistance (Rct) symbolizes the obstacles encountered by electrons during the electrochemical oxidation process. A higher charge transfer resistance implies a lower OER performance. The data from EIS is typically represented graphically through Nyquist plot. The Nyquist plot is divided into three distinct regions: an intercept on the real axis (indicating solution resistance, Rs), a semicircle in the high-frequency zone (representing charge transfer resistance, Rct), and a linear component over low-frequency zones (depicting Warburg resistance, W). These are demonstrated by the imaginary (Z") and real (Z) parts of the impedances. This comprehensive analysis provides a deeper understanding of the electrochemical processes at play.

4.3.4 Number of electrochemical active sites

The number of electrochemical active sites significantly impacts the performance of electrocatalysts. The quantification number of electrochemically active sites (n) is directly proportional to the integrated voltammetric charge across the entire potential range, and its calculation can be accomplished using the following equation:[105]

$$n = \frac{Q}{4F} \tag{4.12}$$

Where F is the faradaic constant (96500 C mol^{-1}) and the absolute voltammetric charge (Q) can be represented as the following equation:

$$Q = \frac{1}{\vartheta_b}\int_{V_1}^{V_2} IdV \tag{4.13}$$

Where V_1 and V_2 are the potential range of the obtained CV curve and ϑ_b is the potential scan rate. There are several strategies to enhance the electrochemical active sites like doping materials with elements, making hybrid nanostructure, by modifying electrocatalytic surfaces.

4.4 Results and discussion

4.4.1 *In-situ* grown $MoSe_2$ over different substrate as binder free electrodes for OER

In this study, we have explored the hydrothermally synthesized in-situ grown $MoSe_2$ over conducting suberates (conducting carbon paper and Ni foam) as binder-free electrodes for OER. This study delves into the characterization and examination of the electrochemical behavior of $MoSe_2$-CCP and $MoSe_2$-Ni foam based electrodes. To study the OER activity of the prepared samples, we have conducted studies using LSV, EIS and chronoamperometry techniques.

4.4.1.1 Characterization of binder free $MoSe_2$ electrodes

In this study, SEM and TEM study reveals that $MoSe_2$ nanostructures have a well-defined, highly dense vertically grown wrinkled architecture with uniform distribution over CCP and Ni foam substrates, as shown in **Figure 3.3** of chapter 3. These electrodes were also characterized by XRD, Raman, FTIR and XPS techniques, as discussed in **Figure 3.4** of chapter 3. They clearly indicate the uniform $MoSe_2$ phase over both substrates. The XPS results (**Figure 3.5**) showed that the $MoSe_2$ grown on CCP mainly consists of the semiconducting 2H phase (80%) with a small amount of the metallic 1T phase (20%), while the $MoSe_2$ grown on Ni foam has more metallic 1T phase (34%) and semiconducting 2H phase (66%). This difference in the phase composition may lead to different catalytic responses of the two electrodes.

4.4.1.2 Electrochemical characterization

OER activity in basic medium

In OER study, we perform LSV measurements of $MoSe_2$-Ni foam and $MoSe_2$-CCP in 1M KOH solution to investigate their electrocatalytic response. Additionally, we have performed LSV for bare Ni foam and bare CCP to understand the OER response of the substrate. We have also examined the OER response of well-known electrocatalyst i.e. RuO_2

as electrode for comparison. The reactions involved in OER process in the basic medium are given in **equation 4.7-4.10**. Low values of overpotential and Tafel slope suggest the high electrocatalytic activity of any material [68]. The Tafel slope is obtained by fitting LSV curves using the following **equation 3.18**. The corresponding Tafel plots are shown in **Figure 4.2 (b)**. The $MoSe_2$-Ni foam electrode shows the pre-oxidation anodic peak at ∼1.5 V, attributed to the oxidation of Ni^{2+} to Ni^{3+} [132-134]he bare Ni foam also exhibit peroxidation peak. The $MoSe_2$-Ni foam shows better electrochemical performance (η_{50} ~377 mV, Tafel slope ~38 mV dec^{-1} in the potential range of 1.3 to 1.36 V vs RHE and Tafel slope~ 420 mV dec^{-1} in the potential range of 1.52 to 1.59 V vs RHE) than $MoSe_2$-CCP (η_{10} ~310 mV, η_{50} ~353 mV and Tafel slope ~45 mV dec^{-1}), bare carbon paper (η_{10} ~630 mV and Tafel slope ~355 mV dec^{-1}), in 1M KOH at potential sweep rate of 2 mV s^{-1}. Both electrodes show better OER performance than well-known electrocatalysts like RuO_2 (η_{10} ~326 mV and Tafel slope ~50 mV dec^{-1}). The EIS for both electrodes are studied at a constant potential of 1.6 V vs. RHE for a better understanding of the OER kinetics, as shown in **Figure 4.2 (c)**. The findings of both electrocatalysts revel the semicircle behavior and are fitted with $R_S(Q_1R_1)(Q_2R_{CT})$, where R_S ~ series resistance (total internal resistance including solution, electrodes and other components), R_1 ~resistance due to microscopic surface roughness, R_{CT} ~charge transfer resistance, and Q_1/Q_2 ~constant-phase parallel components [135]he $MoSe_2$-Ni foam has lower R_S and R_{CT} (R_S~1.9 Ω and R_{CT}~1.4 Ω) values than $MoSe_2$-CCP (R_S~1.4 Ω and R_{CT}~4.5 Ω), beneficial for higher reaction kinetics and low OER overpotential. The iR (90%) compensated LSV curves and corresponding Tafel slopes for both electrodes are shown in **Figure 4.2 (d, e).** Currently, the majority of OER studies of electrocatalysts are determined by the overpotential at anodic current density of 10 mA cm^{-2}. However, in our case of $MoSe_2$-Ni foam electrode, it's challenging to separate the OER due to oxidation of Ni and adsorption of oxygen species because of the overlapping of these two processes in the potential range of 1.4-1.53 V vs. RHE [136]9]. To overcome this situation, we have estimated the overpotential at the higher current density of 50 mA cm^{-2} to eliminate the effect of oxidation, as suggested in literature [136, 137].

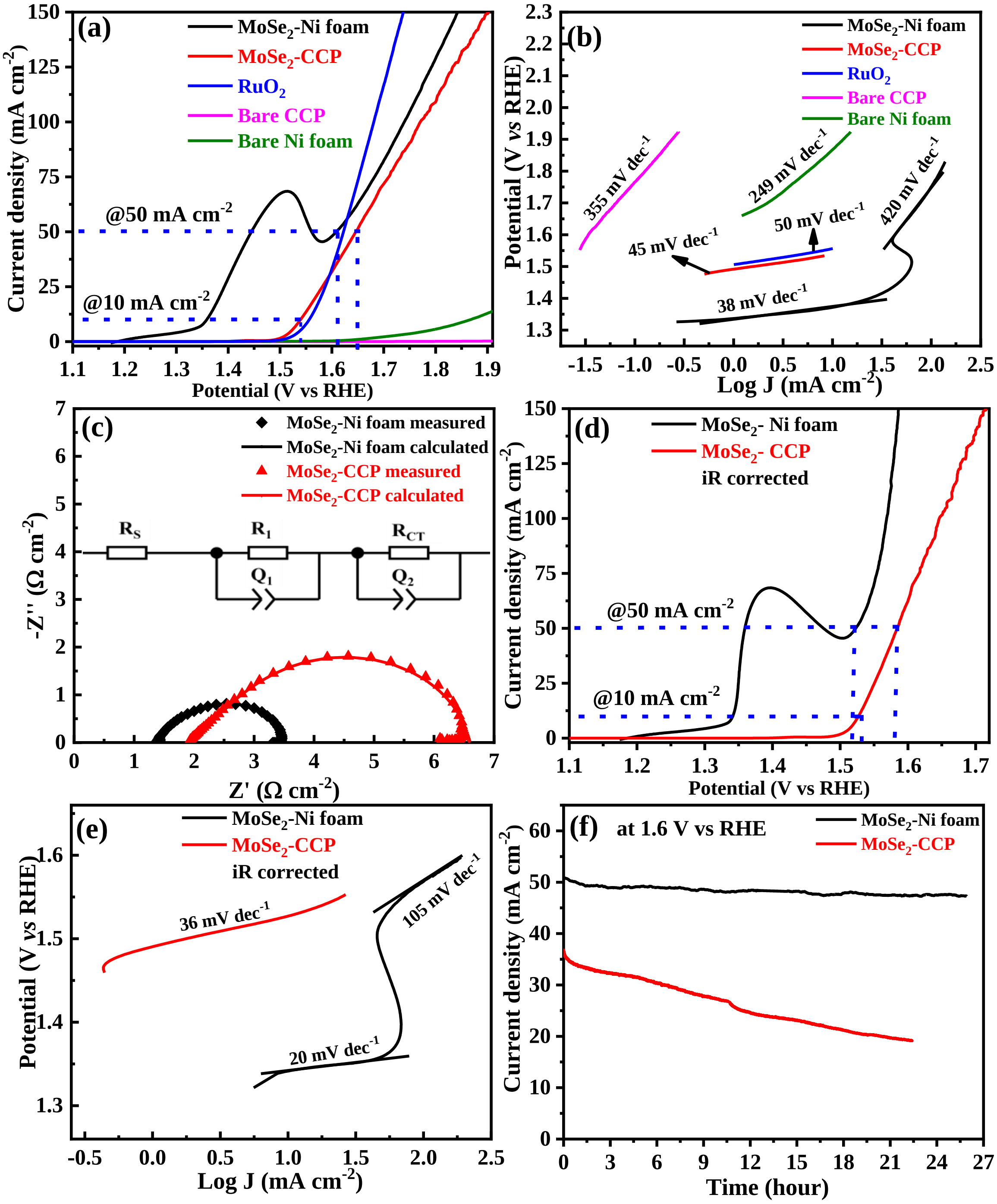

Figure 4.2 *The OER activity of MoSe$_2$-CCP and MoSe$_2$-Ni foam electrodes in 1M KOH electrolyte (a) LSV curves and (b) corresponding Tafel plots at potential sweep rate of 2 mV s^{-1} including for bare substrates and RuO$_2$ (c) EIS curve at constant overpotential ~1.6 V vs RHE, (d) The iR corrected LSV curves, (e) corresponding iR corrected Tafel plots and (f) chronoamperometry study at constant potential ~1.6 V vs RHE.*

The $MoSe_2$-Ni foam shows better electrochemical performance (η_{50} ~292 mV, Tafel slope ~20 mV dec^{-1} in the potential range of 1.3 to 1.36 V vs RHE and Tafel slope~ 105 mV dec^{-1} in the potential range of 1.52 to 1.59 V vs RHE) than $MoSe_2$-CCP (η_{10} ~296 mV, η_{50} ~353 mV and Tafel slope ~36 mV dec^{-1}) in 1M KOH at potential sweep rate of 2 mV s^{-1}. The better OER activity of $MoSe_2$-Ni foam electrode compared to $MoSe_2$-CCP electrode can be attributed to the higher electrochemical active surface area and higher contribution of 1T phase. Long-term stability cum durability is another critical parameter in assessing the practical application of electrocatalysts. Therefore, the stability of the $MoSe_2$ on the Ni foam and CCP is evaluated by the chronoamperometry curves at constant potential ~1.6V vs RHE, as shown in **Figure 4.2 (f)**. The chronoamperometry curve for $MoSe_2$-Ni foam shows the stable current (~93 %) for 24 h, suggesting its higher durability than $MoSe_2$-CCP, which shows ~47% reduction in current during 24 h of operation. The better performance of $MoSe_2$-Ni foam in 1M KOH is due to its high electrocatalytic sites, low contact resistance, and faster charge transfer kinetics.

OER activity in acidic medium

The OER activity of $MoSe_2$-CCP (**Figure 4.3 (a)**) and $MoSe_2$-Ni foam (**Figure 4.3 (b)**) are also conducted in acidic (0.5M H_2SO_4) electrolyte at a potential scan rate of 2 mV s^{-1}. The key reaction steps involved for OER mechanism in the acidic electrolyte are given in **equations 4.2-4.5**. In acidic conditions, OER electrocatalysts exhibit slower reaction kinetics due to hindered electron transfer and proton attachment to oxygen intermediates on the catalyst surface [138]. The inherent instability of catalysts in acidic environments further limits the OER activity. In our case, $MoSe_2$-Ni foam shows extremely poor stability due to the corrosive nature of Ni foam in an acidic medium, while $MoSe_2$-CCP shows some degree of chemical stability but poor OER activity. The EIS and chronoamperometry durability tests of this electrode have not been performed.

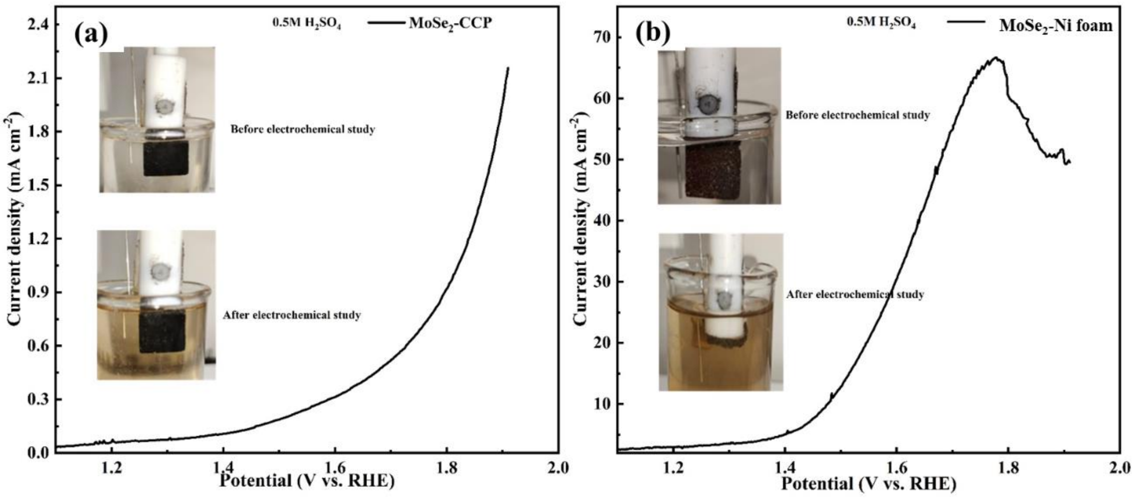

***Figure 4.3** LSV curves of (a) $MoSe_2$-CCP and (b) $MoSe_2$-Ni foam at a scan rate of 2 mV s^{-1} in 0.5M H_2SO_4.*

4.4.2 Pristine $MoSe_2$ as electrocatalyst for OER

In this study, we have explored the hydrothermally synthesized pristine $MoSe_2$ nanosheets as an electrode for OER. This study investigates the electrochemical behavior pristine $MoSe_2$ as an electrode. To assess the OER activity, we have utilized techniques such as LSV, EIS, and chronoamperometry for the durability of the $MoSe_2$ electrode.

4.4.2.1 Electrochemical characterization

The LSV study is performed to understand the OER activity and suitability of electrocatalysts. The LSV curves are fitted with the following Tafel **equation 3.18** to obtain the Tafel slope. In this study, the LSV measurements have been performed in 1 M KOH at scan rates of 2 mVs^{-1} to gather insight into the electrocatalytic activities of pristine $MoSe_2$ for OER study and corresponding LSV curves for prepared samples at the scan rate of 2 mV s^{-1} are shown in **Figure 4.4 (a)**. The pristine $MoSe_2$ shows the overpotential (η_{10}) of 407 mV at the current density of 10 mA cm^{-2}. To further elucidate the OER performance of $MoSe_2$, the corresponding Tafel slope is obtained, as shown in **Figure 4.4 (b)**. The pristine $MoSe_2$ reveals the Tafel slope of 84 mV $decade^{-1}$ at a scan rate of 2 mV s^{-1}. As observed in XPS and Raman studies, the presence of selenium defects may lead to the improvement in number of active sites in $MoSe_2$ [102, 107, 139]. The presence of Se vacancy and edges as active sites and good conductivity of $MoSe_2$ is resulting good electrocatalytic activity of $MoSe_2$ for OER [108].

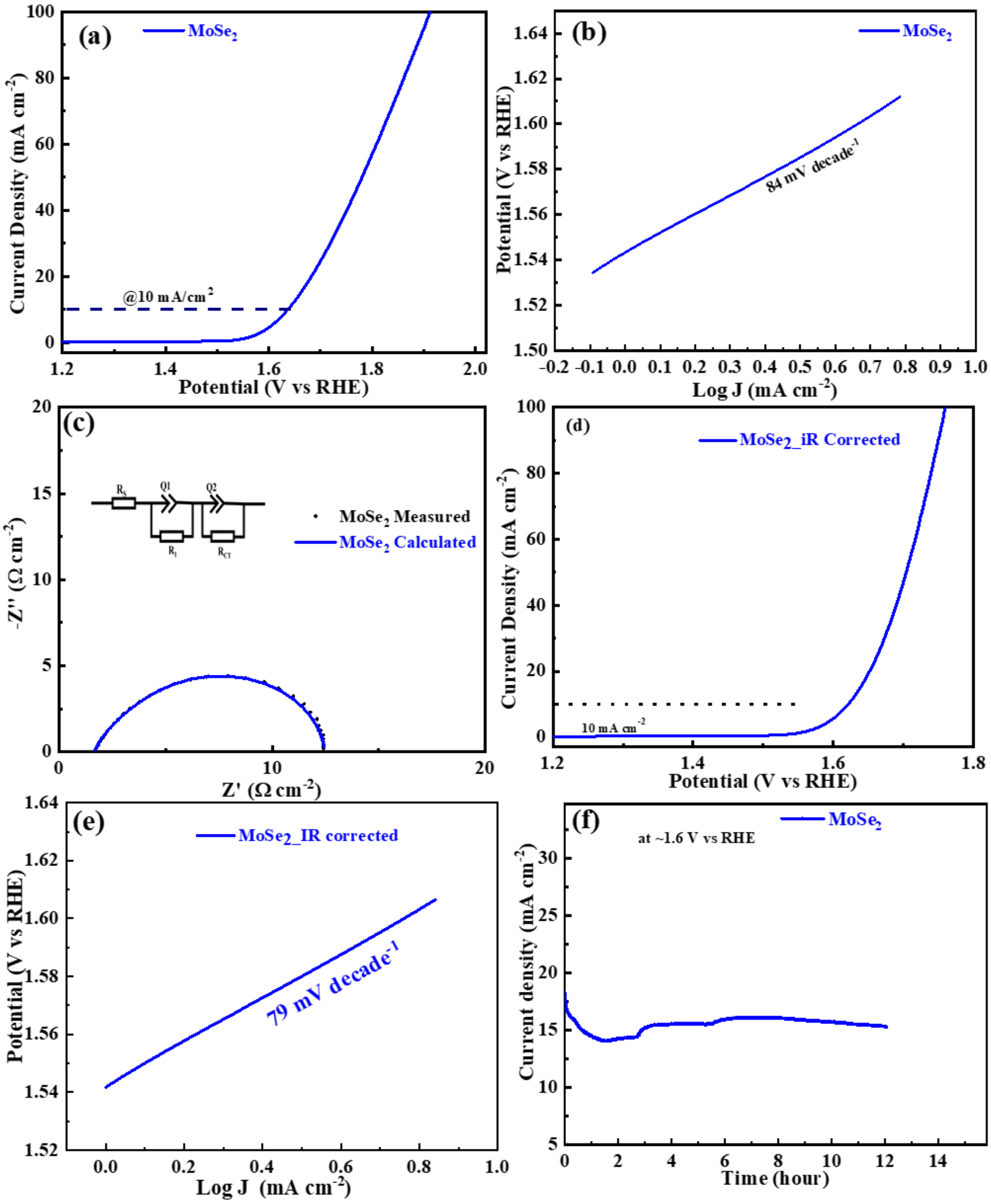

Figure 4.4 *Electrochemcial OER activity of* $MoSe_2$*, (a) LSV curve at a scan rate of 2 mV* s^{-1}*, (b) corresponding Tafel plot, (c) EIS plot at 1.574 V vs RHE, (d) 90% iR corrected OER LSV curve of* $MoSe_2$ *at a scan rate of 2 mV* s^{-1}*, (e) iR corresponding Tafel plot, (f) chronoamperometric curve for prepared sample to observe stability of electrocatalytic activity.*

The EIS study is utilized to evaluate the feasibility of charge transfer on the surface of synthesized electrode materials to further elucidate the OER kinetics. Nyquist plots of pristine

$MoSe_2$ electrocatalysts, reveal semicircle-like curves that are fitted with a $R_S(Q_1R_1)(Q_2R_{CT})$ equivalent circuit model, which include the internal (electrode and electrolyte) resistance (R_S), the resistance due to microscopic surface roughness (R_1), the charge transfer resistance (R_{CT}), and two constant-phase parallel (Q_1, Q_2) components, as shown in **Figure 4.4 (c)** [135]. R_{CT} is closely linked to catalytic kinetics, represent the rate of charge transfer between electrocatalyst and electrolyte. Low R_{CT} values are widely recognized to result in rapid charge transfer kinetics. The low R_S (~1.7 **Ω**) and R_{CT} (~8.5 **Ω**) values for the pristine $MoSe_2$ nanosheets indicates good catalytic activity. In order to evaluate the true electrocatalytic performance of prepared materials, iR correction is incorporated for uncompensated resistance. The LSV polarization curves at a scan rate of 2 mV s^{-1} after 90% iR correction, and corresponding Tafel plot is shown in **Figure 4.4 (e)**. After 90% iR correction, $MoSe_2$ shows overpotential η_{10} of ~391 mV and Tafel's slope of ~79 mV dec^{-1}. To further evaluate the durability of $MoSe_2$ electrocatalyst, chronoamperometry at ~1.6 V vs. RHE has been performed, as shown in **Figure 4.4 (f)**. It indicates constant current density up to 12 h.

In order to understand the electrocatalytic behavior of prepared materials, ECSA analysis is performed using the cyclic voltammetry technique [77, 123]. Under a non-faradaic region of 1.2 and 1.25 V (versus RHE), a series of CV scans have been performed at different scan rates (20, 40, 60, 80 and 100 mV s^{-1}) for $MoSe_2$ as shown in **Figure 4.5 (a)**. To calculate double-layer capacitance (C_{dl}), the half of the average difference between the average of the anodic and cathodic charging current densities at 1.225 V vs RHE are linearly plotted as a function of scan rates and the slope provides the C_{dl} value [124]. It shows the C_{dl} value of $MoSe_2$ ~12.8 mF cm^{-2} equivalent to 3.05 mF cm^{-2} per mg, as shown in **Figure 4.5 (b)**. The ECSA is directly proportional to C_{dl}, and hence high C_{dl} value pristine of $MoSe_2$ suggests good electrocatalytic activity for OER application. Number of active sites (n) is proportional to integrated voltammetric charge over whole range and can be calculated using **equation 4.12**

[140]. The absolute voltammetric charge (Q) can be derived using **equation 4.13** [105]. The Q values, obtained at the scan rate of 20 mV s^{-1}, is found to be 1.4×10^{-3} C for $MoSe_2$. As for calculated Q, the number of active sites (n) are found to be 3.7×10^{-9} mol ($\sim7.6\times10^{-10}$ mol mg^{-1}) for $MoSe_2$. Hence the having significant OER performance of $MoSe_2$ can be used as cathode material for a rechargeable zinc-air battery.

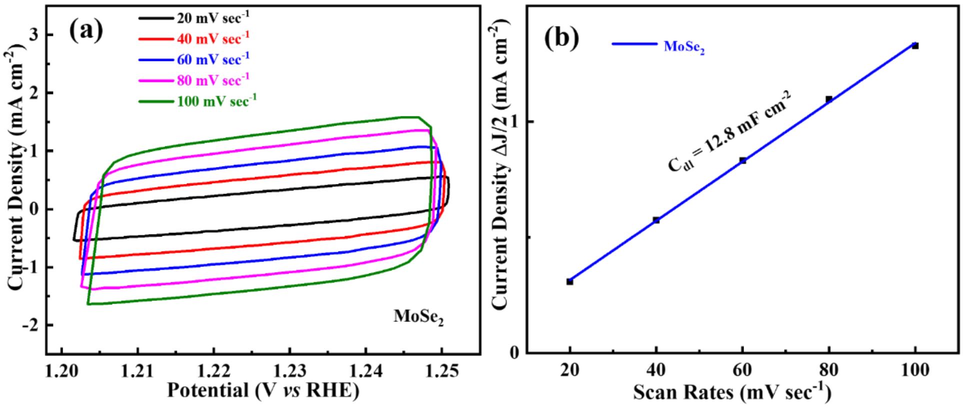

Figure 4.5 *(a) CV curves at different scan rates, (b) ΔJ/2=(Ja-Jc)/2 current density plotted against different potential sweep rates for pristine* $MoSe_2$ *nanosheets.*

4.4.3 Ni decorated $MoSe_2$ as electrode for OER

In this study, we have explored Ni decoration over $MoSe_2$ as electrocatalysts for OER. This study investigates the electrochemical behavior of Ni decoration over $MoSe_2$ coated on CCP as an electrode. To assess the OER activity, we have utilized techniques such as LSV, EIS, and chronoamperometry for the durability of the $MoSe_2$ electrode.

4.4.3.1 Electrochemical characterization

To assess the OER activity, we have utilized techniques such as LSV, EIS, and chronoamperometry for the durability of the Ni-$MoSe_2$ nanocomposites based electrodes.

OER activity in basic medium

The LSV curves for OER catalytic activity of Ni nanoparticle decorated over $MoSe_2$ nanocomposites- Ni-$MoSe_2$ (5%), Ni-$MoSe_2$ (10%) and Ni-$MoSe_2$ (20%) in 1M KOH at a potential sweep rate of 2 mV s^{-1} are shown in **Figure 4.6 (a)**. The key reaction steps involved for OER mechanism in the basic electrolyte are given in **equations 3.14-3.16**. The Ni-$MoSe_2$ (10%) exhibits a lowest η_{10} ~287 mV and Tafel slope ~60 mV dec^{-1} than Ni-$MoSe_2$ (20%) (η_{10} ~300 mV and Tafel slope ~64 mV dec^{-1}) and Ni-$MoSe_2$-Ni (5%) (η_{10} ~317 mV and Tafel slope ~76 mV dec^{-1}), as shown in **Figure 4.6 (b)**. The Ni-$MoSe_2$ (10%) exhibits best OER performance among pristine $MoSe_2$ and Ni-$MoSe_2$ nanocomposites. The EIS Nyquist plots are generated to investigate the OER kinetics of electrodes in basic medium at a constant voltage of 1.6 V vs. RHE. as shown in **Figure 4.6 (c)**. It shows the lower R_{CT} (~4.0 Ω) for Ni-$MoSe_2$ (10%) compared to Ni-$MoSe_2$ (20%) (R_{CT} ~ 10.0 Ω) and Ni-$MoSe_2$ (5%) (R_{CT} ~14.0 Ω) suggesting better electrocatalytic of $MoSe_2$-Ni-10 due to the optimal decoration of Ni over $MoSe_2$, which provide higher synergistic effect between them. **Figure 4.6 (d)** shows the iR (90%) compensated LSV curves at a potential sweep rate of 2 mV s^{-1} and **Figure 4.6 (e)** provides the corresponding iR corrected Tafel plots. After iR correction, the $MoSe_2$-Ni-10 shows even lower η_{10} ~277 mV and Tafel slope ~53 mV dec^{-1} compared to Ni-$MoSe_2$ (20%) (η_{10} ~ 293 mV, Tafel slope ~57 mV dec^{-1}) and Ni-$MoSe_2$ (5%) (η_{10} ~ 306 mV, Tafel slope ~ 66 mV dec^{-1}). The chronoamperometry experiment at a constant overpotential of 1.6V vs. RHE characterizes the stability and durability of Ni-$MoSe_2$ nanocomposites based electrodes, as shown in **Figure 4.6 (f)**. The Ni-$MoSe_2$ (10%) electrode shows better catalytic stability (current retention ~91%) for 24 h of continuous operation compared to Ni-$MoSe_2$ (20%) (~85%) for 24 h and Ni-$MoSe_2$ (5%) (~81%) for 22 h. The number of active sites (n) is proportional to integrated voltammetric charge over whole range and can be calculated using **equation 4.2** [140]. The absolute voltammetric charge (Q) can be derived using **equation 4.3** [141] . The Q values, obtained at the scan rate of 20 mV s^{-1}, are found to be 1.1×10^{-2} C, 1.3×10^{-2} C, and 1.2×10^{-2} C for Ni-$MoSe_2$ (5%), Ni-$MoSe_2$ (10%), and Ni-$MoSe_2$ (20%) nanocomposite, respectively. The number of active sites (n) are found to be 2.7×10^{-8} mol (~7.0×10^{-9} mol mg^{-1}) for Ni-$MoSe_2$ (5%), 3.4×10^{-8} mol (~1.1×10^{-8} mol mg^{-1}) for Ni-$MoSe_2$ (10%), and 3.1×10^{-8} mol

(9×10^{-9} mol mg^{-1}) for Ni-MoSe$_2$ (20%) nanocomposites. It suggests that the number of active sites for Ni-MoSe$_2$ (10%) nanocomposites is higher than Ni-MoSe$_2$ (5%) and Ni-MoSe$_2$ (20%) nanocomposites, indicating higher catalytic activity. The higher OER activity for Ni-MoSe$_2$ (10%) is due to the optimum presence of Ni nanoparticles over MoSe$_2$. It provides a high synergistic effect between Ni nanoparticle and pristine MoSe$_2$ compared to Ni-MoSe$_2$ (20%) and Ni-MoSe$_2$ (5%).

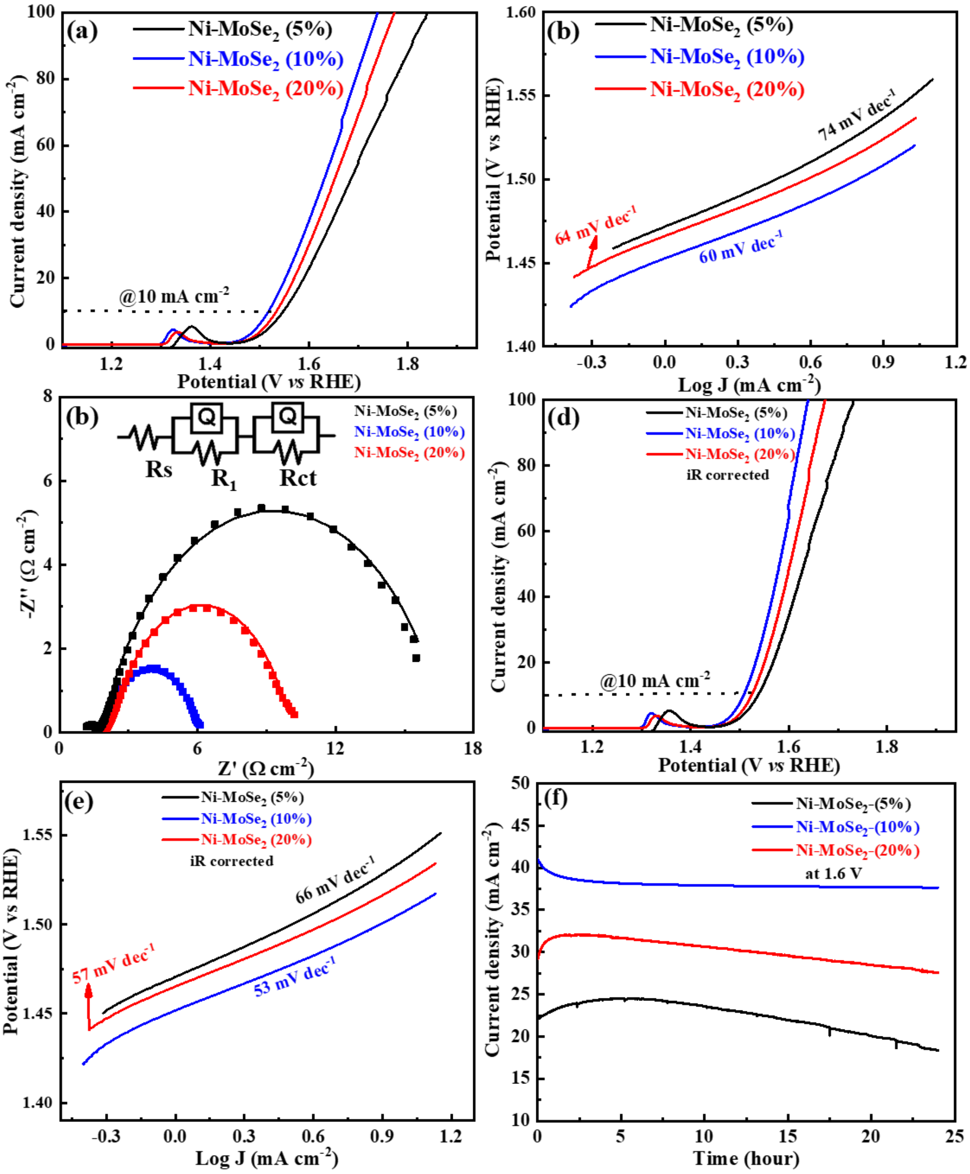

Figure 4.6 *The OER activity of Ni-MoSe$_2$ (5%), Ni-MoSe$_2$ (10%) and Ni-MoSe$_2$ (20%) nanocomposites in 1M KOH electrolyte (a) LSV curves and (b) corresponding Tafel plots at potential sweep rate of 2 mV s^{-1}, (c) EIS curve at constant overpotential ~1.6 V vs RHE, (d) The iR corrected LSV curves, (e) corresponding iR corrected Tafel plots and (f) chronoamperometry study at constant potential ~1.6 V vs RHE.*

4.4.4 $NiCo_2O_4$/NiO-$MoSe_2$ hybrid nanostructure as electrode for OER

In this study, we have explored the hydrothermally synthesized $NiCo_2O_4$/NiO-$MoSe_2$ hybrid nanostructure and pristine $NiCo_2O_4$/NiO as electrocatalyst for OER. This study delves into the characterization and examination of the electrochemical behavior of $MoSe_2$ hybrid nanostructure and pristine $NiCo_2O_4$/NiO materials. To study the OER activity of the prepared samples, we have conducted studies using LSV, EIS and chronoamperometry. Additionally, CV techniques have been employed to determine the ECSA.

4.4.4.1 Characterization of $NiCo_2O_4$/NiO-$MoSe_2$ hybrid nanostructure

In order to understand the morphology and structure of prepared materials, electron microscopy studies are performed. SEM (**Figure 4.6 (a)**) and TEM (**Figure 4.7 (b, c)**) images of $NiCo_2O_4$/NiO indicate the formation of nanoclusters with varying dimensions of less than 100 nm. SEM image (**Figure 4.7 (d)**) clearly indicates the uniform presence of wrinkled $MoSe_2$ nanosheets and $NiCo_2O_4$/NiO in $NiCo_2O_4$/NiO-$MoSe_2$ hybrid nanostructure. TEM images (**Figure 4.7 (e,f)**) reveal the conjoint nature of $MoSe_2$ and $NiCo_2O_4$/NiO in hybrid nanostructure, suggesting the homogeneity of hybrid nanostructure.

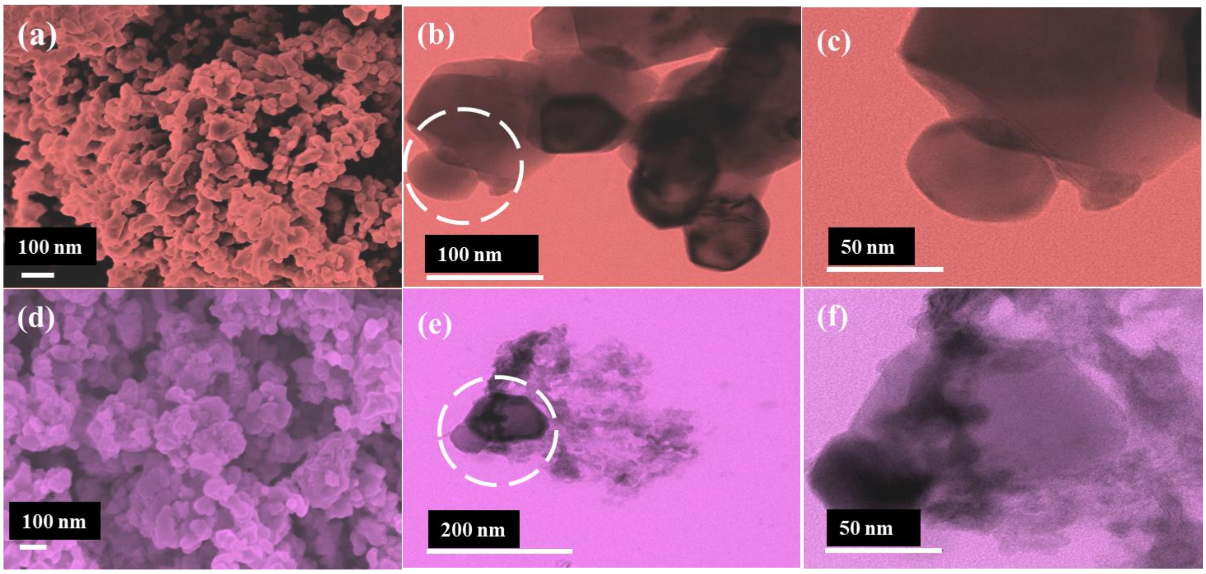

***Figure 4.7** SEM, TEM and higher magnification TEM images of (a-c) $NiCo_2O_4$/NiO and (d-f) $NiCo_2O_4$/NiO-$MoSe_2$ hybrid nanostructure, respectively.*

The XRD study confirms the phase and purity of $NiCo_2O_4$/NiO, and $NiCo_2O_4$/NiO-$MoSe_2$ hybrid nanostructure, as shown in **Figure 4.8 (a)**. The XRD pattern of $NiCo_2O_4$/NiO nanocluster indicates two phase structure with the presence of diffraction peaks at 19.1°, 31.3°, 36.8°,38.5, 44.8°, 55.64°,59.3°, 65.2°, and 77.3° corresponding to different (h k l) planes of $NiCo_2O_4$ (JCPDS no. 20-0781) and peaks located at 37.2°, 43.2°, 62.8°,75.3, and 79.2°, corresponds to (h k l) planes of NiO (JCPDS no. 04-0835) [142, 143]. The XRD pattern of the $NiCo_2O_4$/NiO-$MoSe_2$ hybrid nanostructure shows the presence of all peaks corresponding to both $MoSe_2$ and $NiCo_2O_4$/NiO, indicating the formation of the hybrid nanostructure. Raman and FTIR studies are performed to understand the vibrational characteristics of prepared samples. **Figure 4.8 (b)** shows the Raman spectra for prepared samples. Raman spectrum of $NiCo_2O_4$/NiO shows peaks at 190.4, 471.4, 517.6, and 672.6 cm^{-1} corresponding to F_{2g}, E_g, LO, and A_{1g} modes of $NiCo_2O_4$. One phonon mode of LO for NiO is merged with the peak at LO mode of $NiCo_2O_4$ in as-synthesized $NiCo_2O_4$/NiO [144]. Raman spectrum of $NiCo_2O_4$/NiO-$MoSe_2$ hybrid nanostructure shows the peaks at F_{2g}~185.6 cm^{-1}, E_g~465.6 cm^{-1}, LO~509.5 cm^{-1}, A_{1g}~664 cm^{-1} belonging to $NiCo_2O_4$/NiO and A_{1g}~239.4 cm^{-1} and E^1_{2g}~ 282.8 cm^{-1} belonging to $MoSe_2$. The significant shift in Raman modes of $NiCo_2O_4$/NiO-$MoSe_2$ hybrid nanostructure compared to pristine $MoSe_2$ and $NiCo_2O_4$/NiO clearly indicates good interaction. This clearly suggests the formation of homogeneous hybrid nanostructure. FTIR spectra, shown in **Figure 4.8 (c)**, indicate the presence of different functional groups in prepared samples. FTIR spectrum of $NiCo_2O_4$/NiO shows two strong peaks at 573 and 660 cm^{-1}, attributed to the tensile vibrations of metal oxides. Peaks around 1630 and 3410 cm^{-1}, corresponding to H-O-H bending and O-H stretching under weak hydrogen bonds, respectively [74, 113]. The hybrid nanostructure clearly shows the vibrational modes, belonging to $MoSe_2$ and $NiCo_2O_4$/NiO with some degree of peak shifting compared to pristine ones, again indicating good interaction between them in the hybrid nanostructure.

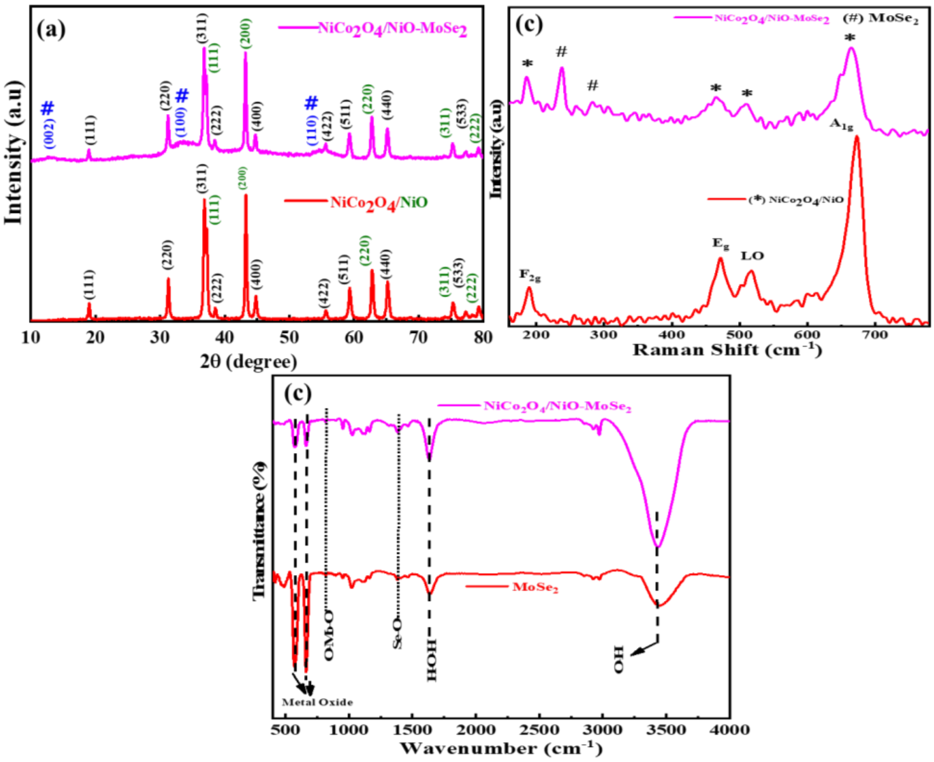

Figure 4.8 *(a) XRD patterns (b) Raman and (c) FTIR spectra of $NiCo_2O_4/NiO$ and $NiCo_2O_4/NiO-MoSe_2$ hybrid nanostructure.*

The composition analysis of $NiCo_2O_4/NiO-MoSe_2$ hybrid nanostructure is performed by XPS. **Figure 4.9 (a)** depicts the survey spectrum of $NiCo_2O_4/NiO-MoSe_2$ hybrid nanostructure, which reveals the existence of characteristic peaks of Mo 3d, Se 3d, Ni 2p, Co 2p, O, and C (carbon peak is due to used carbon reference in measurement). The XPS signal of Mo 3d (**Figure 4.9 (b)**) indicates peaks at ~228.22 eV ($3d_{5/2}$) and ~231.56 eV ($3d_{3/2}$) corresponding to Mo^{4+}, while peaks at ~232.48 eV ($3d_{5/2}$) and ~235.49 eV ($3d_{3/2}$) belong to Mo^{6+} [120]. The Se core level XPS spectrum (**Figure 4.9 (c)**) shows two distinct peaks at ~53.72 eV for Se $3d_{5/2}$ and ~54.58 eV for Se $3d_{3/2}$, indicating that selenium exists as Se^{2-} state. Peaks at ~59.71 eV and ~61.35 eV are attributed to $Se^{+4,}$ possibly due to partial oxidation of Se edges [114, 121, 122]. Peaks of the Ni 2p spectrum are fitted to two spin-orbit doublets and two shakeup satellite peaks, as shown in **Figure 4.9 (d)**. Binding energies of ~854.06 (Ni^{3+}) and ~855.78 eV (Ni^{2+}) are ascribed to Ni $2p_{3/2,}$ whereas peaks with binding energies of ~871.46 (Ni^{3+}) and ~873.26 eV (Ni^{2+}) are assigned to Ni $2p_{1/2}$ peaks. Likewise, the peaks of Co 2p spectra are fitted to two high-resolution spin-orbit doublets and two satellite peaks, as illustrated in **Figure 4.9 (e)**. The spin-orbit doublets with binding energies of ~779.29 and ~794.66 eV are ascribed to Co^{3+} species, while peaks at ~780.72 and ~796.22 eV are associated to Co^{2+} species [144-146]. Only two contributions are seen in O 1s spectra designated as O1 at ~529.6 eV and O2 at ~531.2 eV (**Figure 4.9 (f)**). The peak at ~529.6 eV attribute to the presence of metal oxide, and the peak at ~531.2 eV is usually associated with defects or oxygen ions in low coordination [144, 147]. These findings reveal that the surface composition of as-synthesized $NiCo_2O_4$/NiO-$MoSe_2$ hybrid nanostructure includes Mo^{4+}, Mo^{6+}, Ni^{2+}, Ni^{3+} Co^{2+}, Co^{3+}, and O.

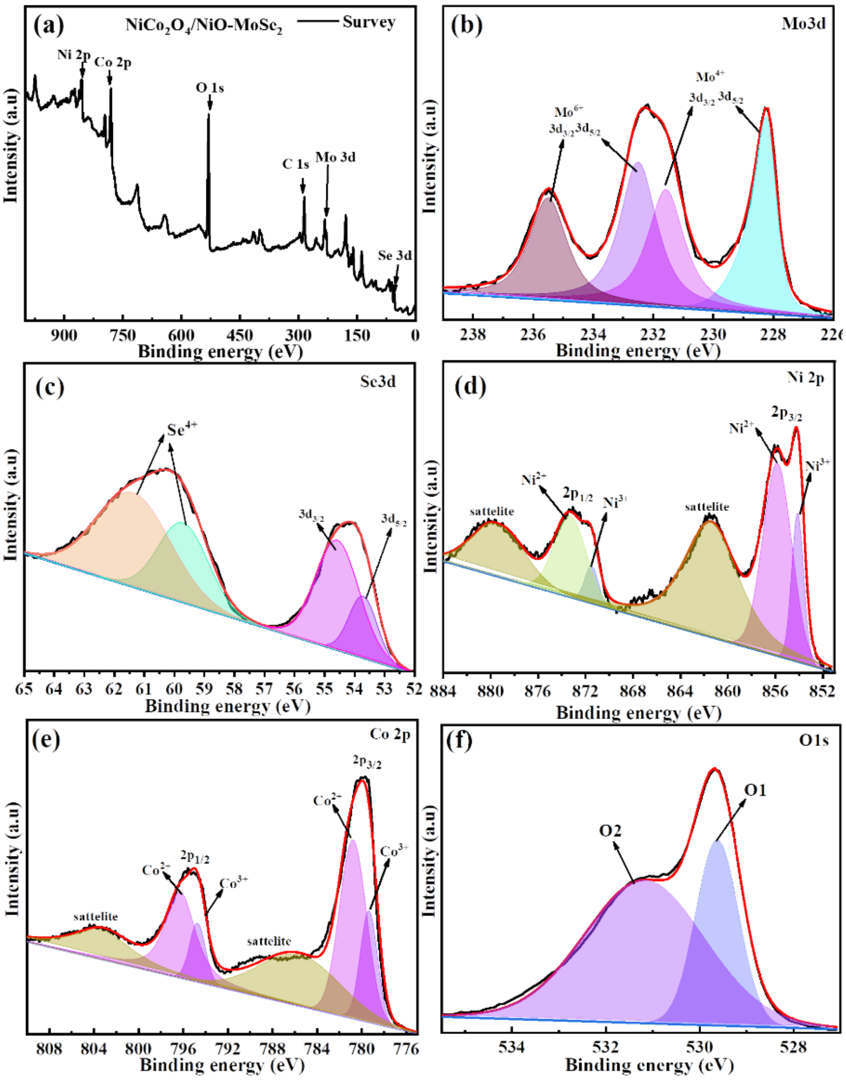

Figure 4.9 *XPS spectra of $NiCo_2O_4$/NiO-$MoSe_2$ hybrid nanostructures (a) Survey spectrum; Spectrum for (b) Mo 3d, (c) Se 3d, (d) Ni 2p, (e) Co 2p, and (f) O1s.*

4.4.4.2 Electrochemical characterization

To assess the OER activity, we have utilized techniques such as LSV, EIS, and chronoamperometry for the durability of the $NiCo_2O_4/NiO-MoSe_2$ hybrid nanostructure electrode.

OER activity in basic medium

The LSV study is performed to understand the OER activity. The LSV curves are fitted with the Tafel **equation 3.17** to obtain the Tafel slope. In the present work, the LSV measurements have been performed in 1 M KOH for prepared samples at the scan rate of 2 mV s^{-1}, as shown in **Figure 4.10 (a)**. The $NiCo_2O_4/NiO-MoSe_2$ hybrid nanostructure shows lower overpotential (η_{10}) of 337 mV compared $NiCo_2O_4/NiO$ (418 mV) at the current density of 10 mA cm^{-2}. To further elucidate the OER performance of prepared materials, the corresponding Tafel slopes are obtained, as shown in **Figure 4.10 (b)**. The $NiCo_2O_4/NiO-MoSe_2$ hybrid nanostructure reveals the lower Tafel slope of 61 mV $decade^{-1}$ compared $NiCo_2O_4/NiO$ (86 mV $decade^{-1}$) at a scan rate of 2 mV s^{-1}. The low overpotential ($\eta_{10\sim}$ 337 mV) and low Tafel slope (61 mV $decade^{-1}$) of $NiCo_2O_4/NiO-MoSe_2$ hybrid nanostructure clearly indicates its better OER activity compared to pristine $NiCo_2O_4/NiO$. The presence of Se edges as active sites and good conductivity of $MoSe_2$ is resulting in excellent electrocatalytic activity of $MoSe_2$ for OER, while the OER activity of $NiCo_2O_4/NiO$ is due to abundant active Ni and Co sites participating together [108]. Hence, the better OER performance of $NiCo_2O_4/NiO-MoSe_2$ hybrid nanostructure compared to $NiCo_2O_4/NiO$ can be directly attributed to the synergistic effect between $MoSe_2$ and $NiCo_2O_4/NiO$. Active sites related to Se defects and edges in $MoSe_2$ and active sites of Ni and Co are combinedly responsible for excellent catalytic activity of hybrid nanostructure. We have also compared the OER activity of our prepared catalysts with RuO_2 (η_{10} ~326 mV and Tafel slope ~50 mV dec^{-1}). The EIS study is utilized to evaluate the feasibility of charge transfer on the surface of synthesized electrode materials to further elucidate the OER kinetics. Nyquist plots, corresponding to three studied electrocatalysts, reveal semicircle-like curves that are fitted with a $R_S(Q_1R_1)(Q_2R_{CT})$ equivalent circuit model, which include the internal (electrode and electrolyte) resistance (R_S), the resistance due to microscopic surface roughness (R_1), the charge transfer resistance (R_{CT}), and two constant-phase parallel (Q_1, Q_2) components, as shown in **Figure 4.10 (c)** [135]. It is clear that R_{CT}, which is closely linked to catalytic kinetics, might represent the rate of charge transfer between catalysts and electrolyte.

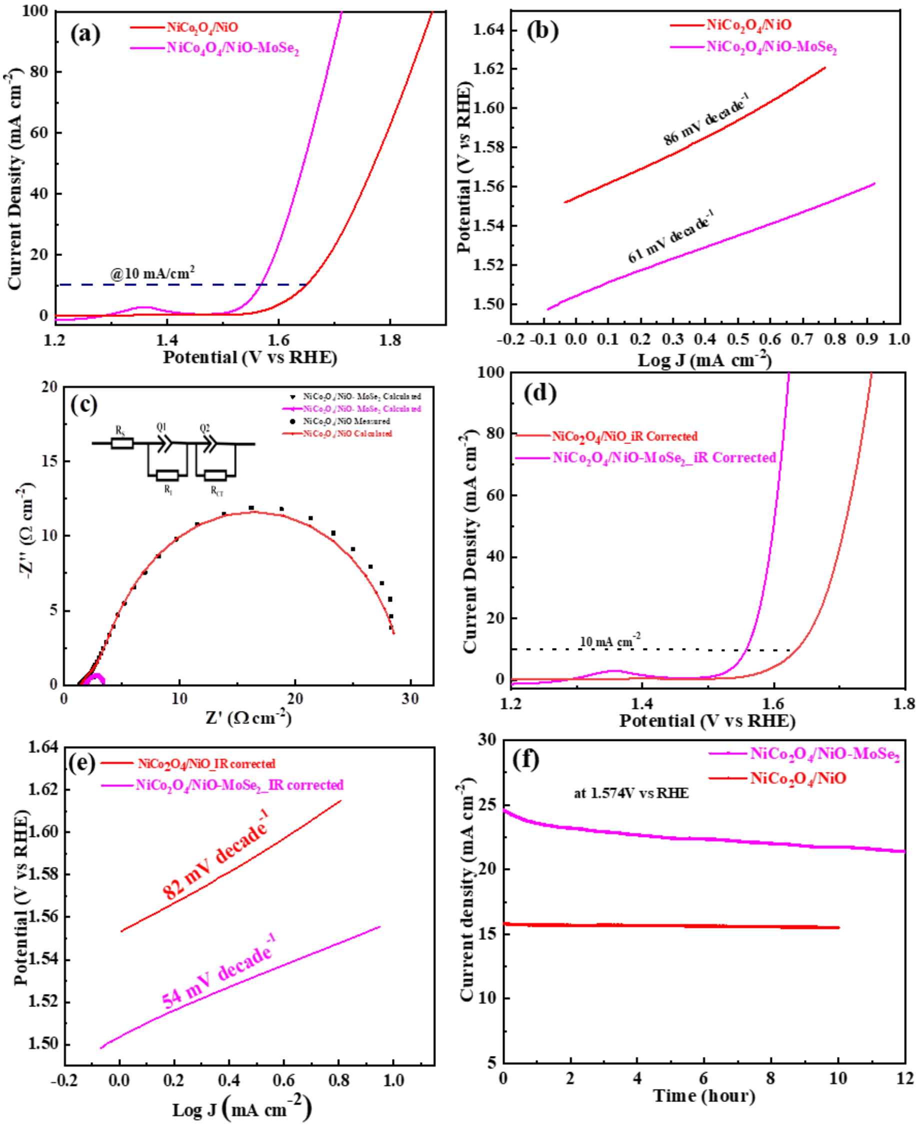

Figure 4.10 *(a) Comparison of the LSV curves of* $MoSe_2$*,* $NiCo_2O_4/NiO$*, and* $NiCo_2O_4$*-*$MoSe_2$ *hybrid nanostructure in 1M KOH at a scan rate of 2 mV* s^{-1} *for OER study, (b) Corresponding Tafel plots, (c) Comparison of EIS plots at 1.574 V vs RHE, (d) iR corrected OER LSV curve, (e) iR corresponding Tafel plots and (f) Chronoamperometric curves for prepared samples to observe stability of electrocatalytic activity.*

Low R_{CT} values are widely recognized to result in rapid charge transfer kinetics. It indicates that $NiCo_2O_4/NiO-MoSe_2$ hybrid nanostructure shows the lower values of R_{CT} (~ 1.7 Ω) compared to $NiCo_2O_4/NiO$ (R_{CT} ~ 25.5 Ω), indicating its better electrocatalytic activity. **Figure 4.10 (d)** shows the LSV polarisation curves at a scan rate of 2 mV s^{-1} after 90% iR correction, and corresponding Tafel plots are shown in **Figure 4.9 (e)**. After 90% iR correction, $NiCo_2O_4/NiO-MoSe_2$ hybrid nanostructure shows lower overpotential (η_{10}~ 328 mV) and Tafel's slope (54 mV $decade^{-1}$) as compared $NiCo_2O_4/NiO$ (η_{10}~405 mV and Tafel's slope~ 83 mV $decade^{-1}$). To further evaluate the durability of prepared electrocatalyst, chronoamperometry at ~1.6 V vs. RHE has been performed for prepared samples, as shown in **Figure 4.10 (f)**. It clearly indicates that higher constant current density is observed for longer duration (~15 h) for $NiCo_2O_4/NiO-MoSe_2$ hybrid nanostructure compared to $NiCo_2O_4/NiO$ (~10 h), indicating the robustness of hybrid nanostructure for OER application.

Electrochemical active surface area

To understand the electrocatalytic behavior of prepared materials, ECSA analysis is performed using the cyclic voltammetry technique [77, 123]. Under a non-faradaic region of 1.2 and 1.25 V (versus RHE), a series of CV scans have been performed at different scan rates (20, 40, 60, 80 and 100 mV s^{-1}) for $NiCo_2O_4/NiO-MoSe_2$ hybrid nanostructure (**Figure 4.11 (a)**) and $NiCo_2O_4/NiO$ (**Figure 4.11 (b)**). To calculate double-layer capacitance (C_{dl}), the half of the average difference between the average of the anodic and cathodic charging current densities at 1.225 V vs RHE are linearly plotted as a function of scan rates and the slope provides the C_{dl} value [124]. It is observed that the $NiCo_2O_4/NiO-MoSe_2$ hybrid nanostructure electrode shows the higher C_{dl} value (55.1 mF cm^{-2} equivalent to 8.7 mF cm^{-2} per mg electrode loading) compared $NiCo_2O_4/NiO$ (8.9 mF cm^{-2} equivalent to 2 mF cm^{-2} per mg), as shown in **Figure 4.11 (c)**.

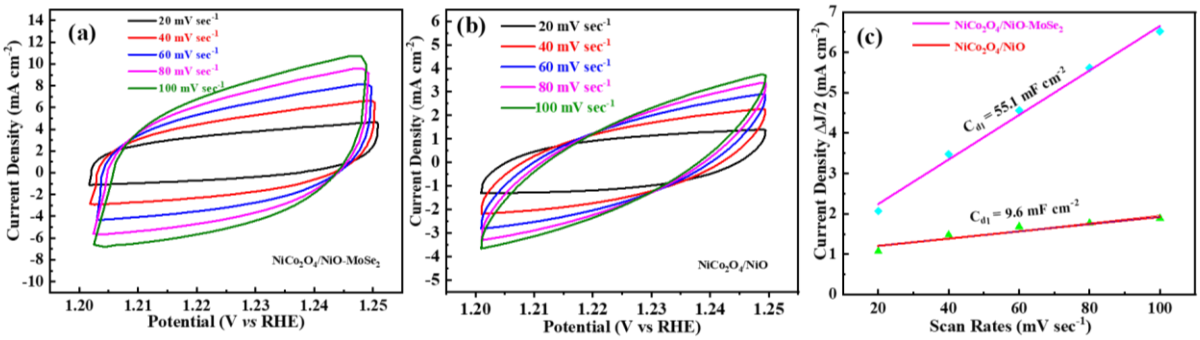

Figure 4.11 *CV curves at different scan rates of (a) $NiCo_2O_4/NiO-MoSe_2$, hybrid nanostructure and (b) $NiCo_2O_4/NiO$; (c) corresponding electrochemical double-layer capacitances (C_{dl}).*

The ECSA is directly proportional to C_{dl}, and hence higher C_{dl} value for $NiCo_2O_4/NiO$ $-MoSe_2$ hybrid nanostructure suggests its better electrocatalytic activity compared to $NiCo_2O_4/NiO$ for OER application. Number of active sites (n) is proportional to integrated voltammetric charge over whole range and can be calculated using **equation 4.2** [140]. The absolute voltammetric charge (Q) can be derived using **equation 4.3** [141]. The Q values, obtained at the scan rate of 20 mV s^{-1}, are found to be 4.2×10^{-3} C, and 1.5×10^{-2} C for $NiCo_2O_4/NiO$, and $NiCo_2O_4/NiO-MoSe_2$ hybrid nanostructure, respectively. As for calculated Q, the number of active sites (n) are found to be 1.1×10^{-8} mol (~2.6×10^{-9} mol mg^{-1}) for $NiCo_2O_4/NiO$, and 3.8×10^{-8} mol (5.9×10^{-9} mol mg^{-1}) for $NiCo_2O_4/NiO-MoSe_2$ hybrid nanostructure. It suggests that the number of active sites (n) for $NiCo_2O_4/NiO-MoSe_2$ hybrid nanostructure is higher than $MoSe_2$ and $NiCo_2O_4/NiO$, indicating higher catalytic activity of hybrid nanostructure.

4.4.5 $CoFe_2O_4-MoSe_2$ hybrid nanostructure as electrode for OER

In this study, we have explored the $CoFeO_4-MoSe_2$ hybrid nanostructure and pristine $CoFeO_4$ as electrocatalysts for OER. This study delves into the characterization and examination of the electrochemical behavior of $CoFeO_4$-$MoSe_2$ hybrid nanostructure and pristine $CoFeO_4$ materials. To study the OER activity of the prepared samples, we have conducted studies using

LSV, EIS and chronoamperometry. Additionally, CV techniques have been employed to determine the ECSA.

4.4.5.1 Characterization of $CoFe_2O_4$-$MoSe_2$ hybrid nanostructure

A typical hydrothermal synthesis process is utilized for $CoFe_2O_4$, and $CoFe_2O_4$-$MoSe_2$ hybrid nanostructure. The prepared electrocatalysts have been investigated using different characterization tools. **Figure 4.12 (a)** show the SEM image of $CoFe_2O_4$ indicating nanoparticle structure. **Figure 4.12 (b)** show the TEM image, clearly indicating particle size in the range 50-100 nm. **Figure 4.12 (c)** depicts SEM image of $CoFe_2O_4$-$MoSe_2$ hybrid nanostructures, indicating the uniform presence of $MoSe_2$ nanosheets and $CoFe_2O_4$ in $CoFe_2O_4$-$MoSe_2$ hybrid nanostructures. **Figure 4.12 (d)** show TEM image, which clearly provides the evidence for interconnected network of $MoSe_2$ and $CoFe_2O_4$ in hybrid nanostructure.

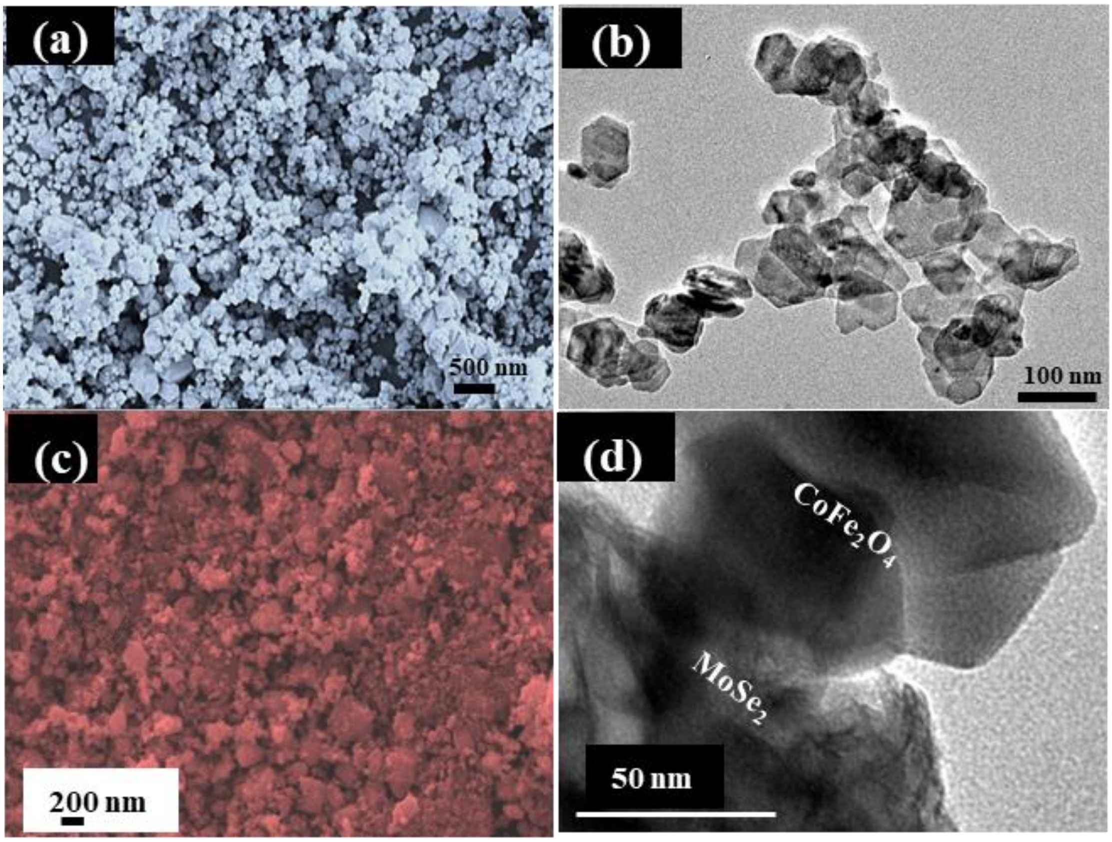

Figure 4.12 *(a,c) SEM and (b.d) TEM images for $CoFe_2O_4$ and $CoFe_2O_4$-$MoSe_2$ hybrid nanostructures, respectively.*

The XRD pattern of $CoFe_2O_4$ reveals distinctive diffraction peaks consistent with the crystallographic planes of cubic spinel $CoFe_2O_4$. Peaks observed at around 18.4°, 30.1°, 35.5°, 37.1°, 43.1°, 53.5°, 55.9°, and 62.6° correspond to the (111), (220), (311), (222), (400), (422), (511), and (440) planes of $CoFe_2O_4$ (JCPDS no. 00-022-1018), as shown in **Figure 4.13 (b)** [41, 148]. The XRD pattern of the $CoFe_2O_4$-$MoSe_2$ hybrid nanostructure displays combined peaks representative of both $CoFe_2O_4$ and $MoSe_2$ phases. Distinctive peaks attributed to $MoSe_2$ are evident, including peaks at around 13.4°, 33.0°, and 55.2°, indicative of its (002), (100), and (110) planes. These peaks confirm the successful formation of the $CoFe_2O_4$-$MoSe_2$ hybrid nanostructure. Both prepared materials show the additional peak around ~44.7° (110), which represents the zero-valent iron (Fe) nanoparticle (JCPDS no. 00-006-0696) [149]. Raman spectra of $CoFe_2O_4$ and $CoFe_2O_4$-$MoSe_2$ hybrid nanostructure are shown in **Figure 4.13 (b)**, exhibiting four clear peaks (T_{2g} (1), E_g, T_{2g} (2) and A_{1g}) corresponding to bimetal oxides. The A_{1g} mode corresponds to the symmetric stretching of oxygen atoms along the bonds between Fe-O and Co-O in the tetrahedral sites. The E_g mode is associated with the symmetric bending of oxygen with respect to metal ion. The T_{2g} (2) mode is caused by the asymmetric stretching of Fe (Co) and O. Lastly, the T_{2g} (1) mode is due to the translational movement of the tetrahedron, which includes the metal ion at the tetrahedral site along with four oxygen atoms [150, 151]. The A_{1g} (~237 cm^{-1}) and E^1_{2g} (~281 cm^{-1}) modes are observed in hybrid nanostructures, belonging to the out-of-plane and in-plane vibrations of $MoSe_2$ [148, 152, 153]. The changes in intensities and Raman shifts for different vibrational modes in $CoFe_2O_4$-$MoSe_2$ hybrid nanostructures compared to pristine $CoFe_2O_4$ can be attributed to the strong interaction between bimetal oxides and $MoSe_2$, indicating the formation of hybrid nanostructure. FTIR spectra, shown in **Figure 4.13 (c)**, indicate the presence of different functional groups in pristine $CoFe_2O_4$ and $CoFe_2O_4$-$MoSe_2$ hybrid nanostructures. FTIR spectrum of $CoFe_2O_4$ show peak at 582 cm^{-1} attributing to tensile vibrations of metal oxide. FTIR spectrum of $CoFe_2O_4$-

$MoSe_2$ hybrid nanostructures shows peaks around 893 and 1625 cm^{-1} corresponding to O-Mo-O and Mo-Se bonds of $MoSe_2$, while the peak at 562 cm^{-1} belongs to metal oxide vibration of $CoFe_2O_4$. Peaks around 3440 cm^{-1} correspond to O-H stretching [74, 113]. The hybrid nanostructure clearly shows the vibrational modes, belonging to $MoSe_2$ and $CoFe_2O_4$ with some degree of peak shifting compared to $CoFe_2O_4$, indicating good interaction between them in the hybrid nanostructure.

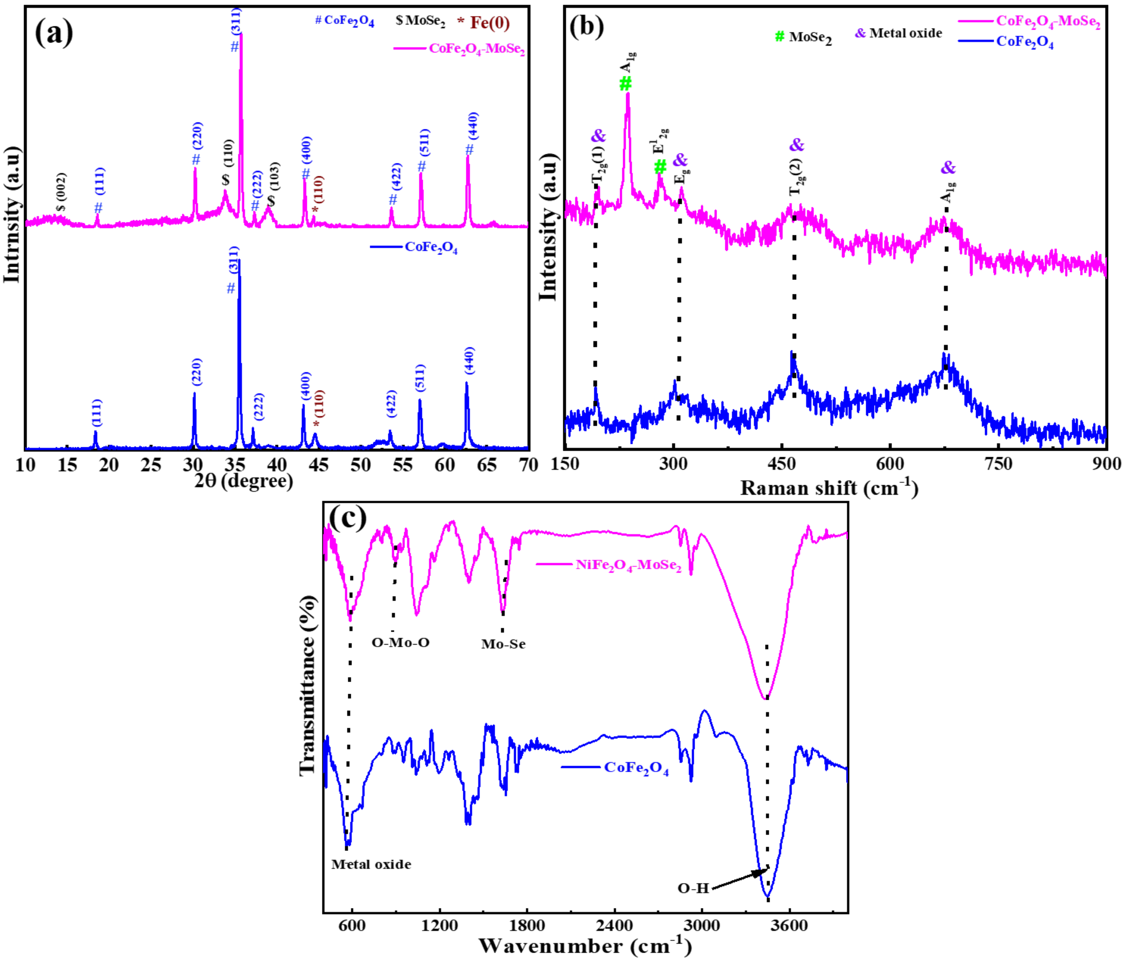

***Figure 4.13** (a) XRD patterns, (b) Raman and (c) FTIR spectra of $CoFe_2O_4$ and $CoFe_2O_4$-$MoSe_2$ hybrid nanostructure.*

The XPS technique provides information about the oxidation states, bonding environments, and electronic properties of the atoms on the surface of prepared materials. The XPS survey spectrum of $CoFe_2O_4$-$MoSe_2$ hybrid nanostructure reveals the presence of Co 2p, Fe 2p, Mo 3d, Se 3d and O 1s states, as shown in **Figure 4.14 (a)**. The Co 2p spectrum (**Figure**

4.14 (b)) displays two spin-orbit doublets and two satellite peaks. The Co $2p_{3/2}$ deconvolute in two binding energies of ~780.3 (Co^{3+}) and ~781.6 eV (Co^{2+}), while Co $2p_{1/2}$ split in ~795.6 (Co^{3+}) and ~797.1 eV (Co^{2+}). The Fe 2p spectrum (**Figure 4.14 (c)**) show four distinctive peaks centered at ~710.8 eV (Fe^{3+} $2p_{3/2}$), ~713.2 eV (Fe^{2+} $2p_{3/2}$), ~724.2 eV (Fe^{3+} $2p_{1/2}$), and ~727.6 eV (Fe^{2+} $2p_{1/2}$) for $CoFe_2O_4$-$MoSe_2$ hybrid nanostructure.

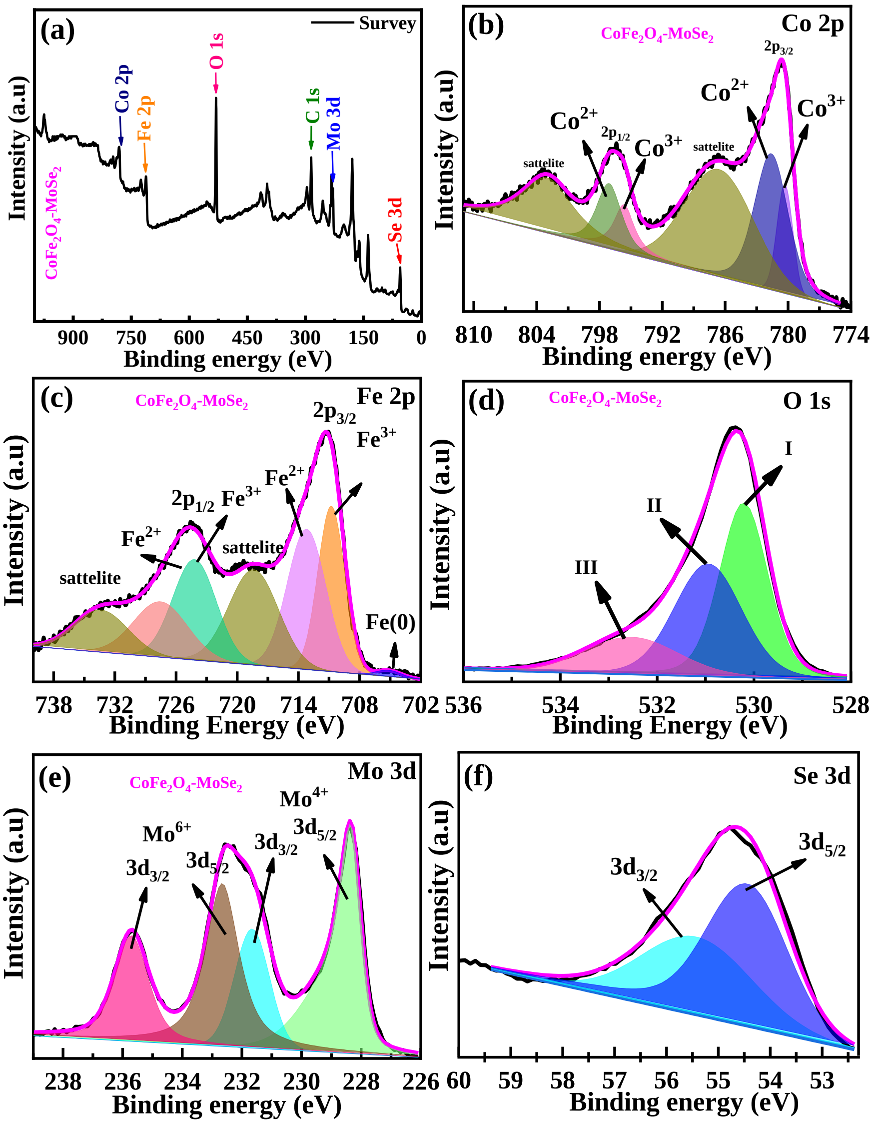

***Figure 4.14** XPS spectra of (a) survey spectra, (b) Co 2p, (c) Fe 2p, (d) O 1s, (e) Mo 3d and (f) Se 3d for $CoFe_2O_4$-$MoSe_2$ hybrid nanostructure.*

A very low intense peak at ~705.1 eV confirms the presence of zero-valent iron Fe(0) in $CoFe_2O_4$-$MoSe_2$ hybrid nanostructures. The O 1s spectra (**Figure 4.14 (d)**) for $CoFe_2O_4$-$MoSe_2$ hybrid nanostructures exhibit three peaks at 530.2 (I), 531.0 (II), and 532.7 eV (III), corresponding to metal oxides, defects or low coordination of oxygen ions and chemisorbed oxygen, respectively [148, 154]. The XPS spectrum (**Figure 4.14 (e)**) of Mo3d for $CoFe_2O_4$-$MoSe_2$ show the peaks at ~228.4 eV ($3d_{5/2}$) and ~231.7 eV ($3d_{3/2}$) belong to Mo^{4+} and peaks at ~232.7 eV ($3d_{5/2}$) and ~235.7 eV($3d_{3/2}$) attribute to Mo^{6+} due to partial oxidation of the Mo in $CoFe_2O_4$-$MoSe_2$. **Figure 4.14 (f)** shows that Se exists in Se^{2-} with peaks at ~54.5 eV (Se $3d_{5/2}$) and ~55.6 eV ($3d_{3/2}$) in $CoFe_2O_4$-$MoSe_2$ [81, 129].

4.4.5.2 Electrochemical characterization

OER activity in basic medium

In this study, we have performed Linear sweep voltammetry (LSV) measurements for OER activity of prepared electrocatalysts in 1M KOH at a potential sweep rate of 2 mV s^{-1}, as shown in **Figure 4.15 (a)**. The $CoFe_2O_4$-$MoSe_2$ hybrid nanostructure shows a lower overpotential (η_{10}) of 234 mV compared to $CoFe_2O_4$ (η_{10} ~279 mV). The LSV curves are fitted with the Tafel Equation to obtain the Tafel slope. The corresponding Tafel slopes (**Figure 4.15 (b)**) of recorded LSV curves show the lower Tafel's slope of 69 mV dec^{-1} for $CoFe_2O_4$-$MoSe_2$ hybrid nanostructure compared to $CoFe_2O_4$ (84 mV dec^{-1}). The high OER electrocatalytic activity of the $CoFe_2O_4$-$MoSe_2$ hybrid nanostructure is primarily attributed to the synergetic effect between $MoSe_2$ and $CoFe_2O_4$. The EIS study is performed in a range of frequencies (10 mHz to 1 MHz) at a constant overpotential, as shown in **Figure 4.15 (c)**. Nyquist plots of prepared electrocatalysts depict the semicircle-like behavior that is fitted with $R_S(Q_1R_1)(Q_2R_{CT})$ equivalent circuit model, which consists of internal resistance (R_S) due to electrode and electrolyte, resistance (R_1) due to microscopic surface roughness, charge transfer resistance (R_{CT}) as encountered by charge carriers (electrons or ions) and two constant phase elements (Q_1, Q_2) as shown in the inset of **Figure 4.15 (c)**. A lower R_{CT} describes that the electrons can move easily across the electrode-electrolyte interface, allowing for faster and more efficient electron transfer during the OER. The $CoFe_2O_4$-$MoSe_2$ hybrid nanostructure has the lower R_{CT} value of 4.25 Ω compared to $CoFe_2O_4$ (60 Ω), again suggesting the better electrocatalytic activity of $CoFe_2O_4$-$MoSe_2$ hybrid nanostructure, as observed in LSV study.

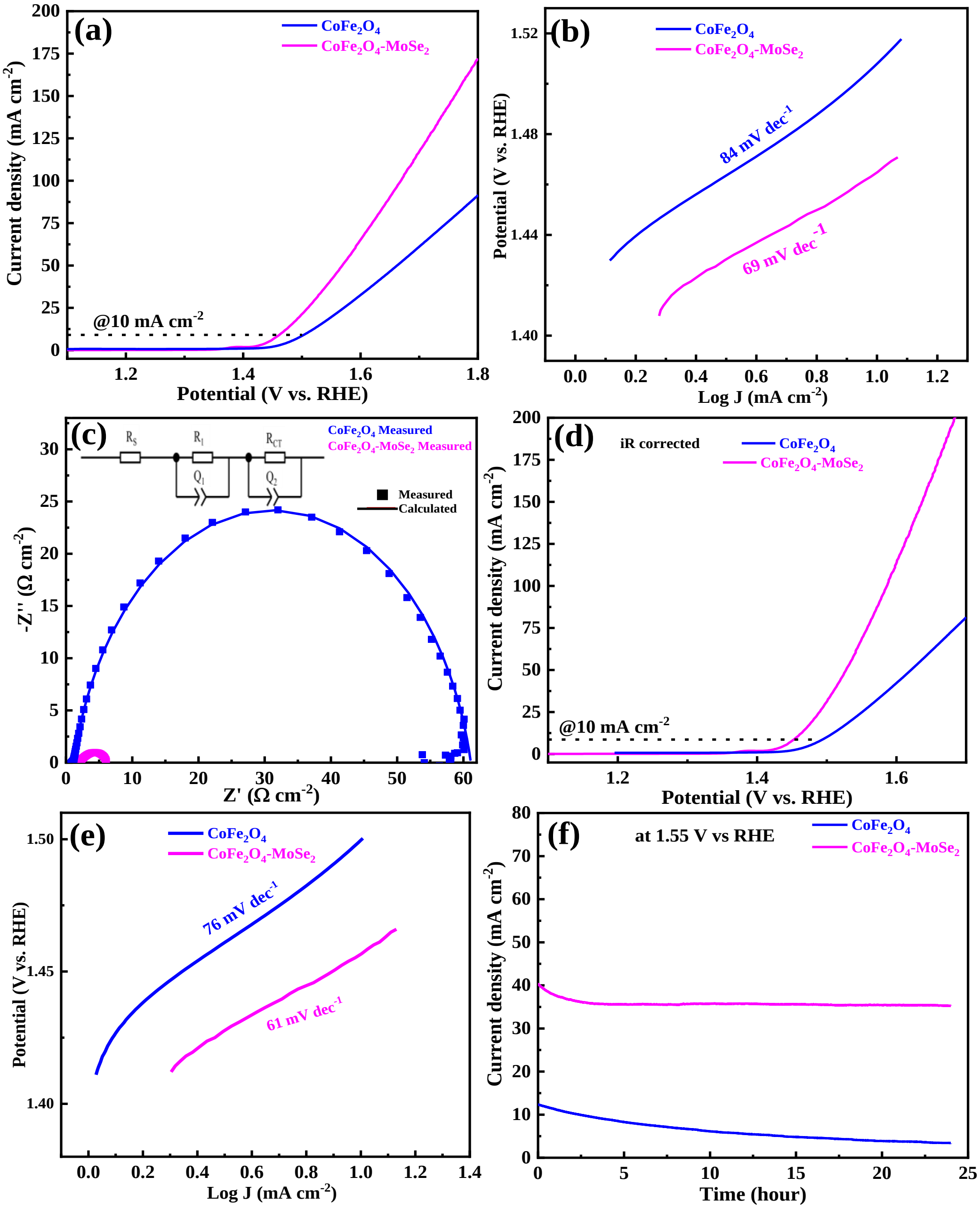

Figure 4.15 *(a) LSV curves, (b) corresponding Tafel plots at potential sweep rates of 2 mV* s^{-1}*, (c) EIS curves, (d) 90% iR corrected LSV curves (e) iR corrected corresponding Tafel plots, (f) Chronoamperometry curves at a constant potential of 1.55 V vs RHE for* $CoFe_2O_4$ *and* $CoFe_2O_4$-$MoSe_2$ *hybrid nanostructure prepared electrocatalysts in 1M KOH.*

The resistance (R_S) of the electrolyte and the electrode-electrolyte interface causes a voltage drop that affects the electrocatalytic performance of the prepared materials. We applied 90%

iR correction to compensate this effect**.** This allows us to obtain the true potential and current values for the OER performance. **Figure 4.15 (d)** shows the 90% iR corrected LSV polarization curves at 2 mV s^{-1}, and **Figure 4.15 (e)** shows the corresponding iR corrected Tafel slopes of prepared materials. The $CoFe_2O_4$-$MoSe_2$ hybrid nanostructure shows the lowest overpotential (η_{10} ~ 226 mV) and Tafel's slope ~61 mV dec^{-1} compared to $CoFe_2O_4$ (η_{10} ~ 269 mV and Tafel slope~ 76 mV dec^{-1}) after iR correction. In order to examine the stability cum durability of electrocatalysts, we have performed chronoamperometry measurement at a constant potential of 1.55 V vs RHE for 24 hours of continuous operation, as shown in **Figure 4.15 (e)**. We observe that the stability curve of $CoFe_2O_4$-$MoSe_2$ hybrid nanostructure shows a high and stable current density (~88 %), suggesting a high degree of durability compared to $CoFe_2O_4$ (~28 %).

The ECSA is an important parameter to understand the electrocatalytic behavior of prepared electrocatalysts. CV is performed by cycling the potential of a working electrode in a non-faradaic region (1.2 to 1.25 V vs RHE) at different potential sweeps (20, 40, 60, 80, 100 mV s^{-1}) for prepared materials, as shown in **Figure 4.16 (a)** for $CoFe_2O_4$ and **Figure 4.16 (b) for** $CoFe_2O_4$-$MoSe_2$ hybrid nanostructure. Half the average difference of anodic and cathodic current densities is linearly plotted versus potential sweep rates, providing C_{dl} value, as shown in **Figure 4.16 (c)**. The $CoFe_2O_4$-$MoSe_2$ hybrid nanostructure shows the higher C_{dl} value (14.6 mF cm^{-2} or 7.0 mF cm^{-2} mg^{-1}) compared to pristine $CoFe_2O_4$ (1.1 mF cm^{-2} or 0.48 mF cm^{-2} mg^{-1}). The ECSA shows a direct correlation with the C_{dl} and hence a greater C_{dl} value for $CoFe_2O_4$-$MoSe_2$ hybrid nanostructure indicates higher ECSA compared to $CoFe_2O_4$ electrocatalysts. We have also calculated the number of electrochemically active sites, as described **equation 4.2-4.3**. The number of active sites (n) are found to be ~0.23×10^{-9} mol mg^{-1} for $CoFe_2O_4$ and ~1.1×10^{-9} mol mg^{-1} for $CoFe_2O_4$-$MoSe_2$ hybrid nanostructure. The hybrid nanostructures show higher number of active sites compared to pristine $MoSe_2$ (0.76×10^{-9} mol mg^{-1}), as reported in our previous section.[22] The reduced agglomeration of nanoparticles and nanosheets in hybrid nanostructures due to probe sonication process provide higher metal active sites and exposed edges of $MoSe_2$ in hybrid nanostructures resulting in higher number of active sites [155-159].

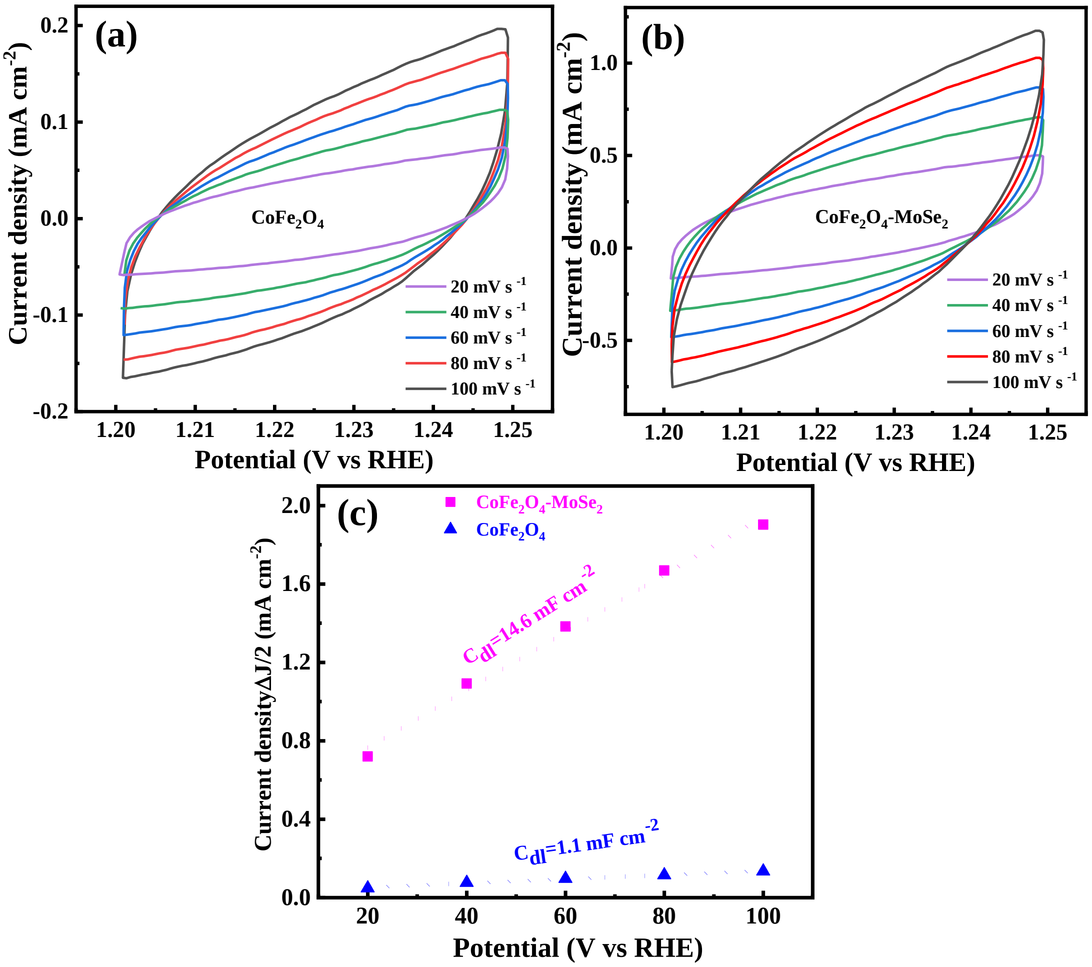

Figure 4.16 *CV curves of (a) $CoFe_2O_4$, (b) $CoFe_2O_4$-$MoSe_2$ hybrid nanostructure at different scan rates and (c) corresponding electrochemical double-layer capacitance (C_{dl}).*

4.4.6 $NiFeO_4$-$MoSe_2$ hybrid nanostructure as electrode for OER

In this study, we have explored the hydrothermally synthesized $NiFeO_4$-$MoSe_2$ hybrid nanostructure and pristine $NiFeO_4$ as electrocatalyst for OER. This study delves into the characterization and examination of the electrochemical behavior of these electrocatalysts. To study the OER activity of the prepared samples, we have performed LSV, EIS and chronoamperometry techniques. Additionally, CV techniques have been employed to determine the ECSA.

4.4.6.1 Characterization of $NiFe_2O_4$-$MoSe_2$ hybrid nanostructure

A typical hydrothermal synthesis process is utilized for $NiFe_2O_4$, and $NiFe_2O_4$-$MoSe_2$ hybrid nanostructure. The prepared electrocatalysts have been investigated using different characterization tools. **Figure 4.17 (a)** show the SEM image of $NiFe_2O_4$ nanoparticles. **Figure 4.17 (b)** show the TEM image clearly indicating the particle size in the range 50-100 nm. **Figure 4.17 (c)** depicts SEM image of $NiFe_2O_4$-$MoSe_2$ hybrid nanostructure, indicating the uniform presence of $MoSe_2$ nanosheets and $NiFe_2O_4$ in $NiFe_2O_4$-$MoSe_2$ hybrid nanostructures. **Figure 4.17 (d)** show TEM image, which clearly provides the evidence for interconnected network of $MoSe_2$ and $NiFe_2O_4$ in hybrid nanostructure.

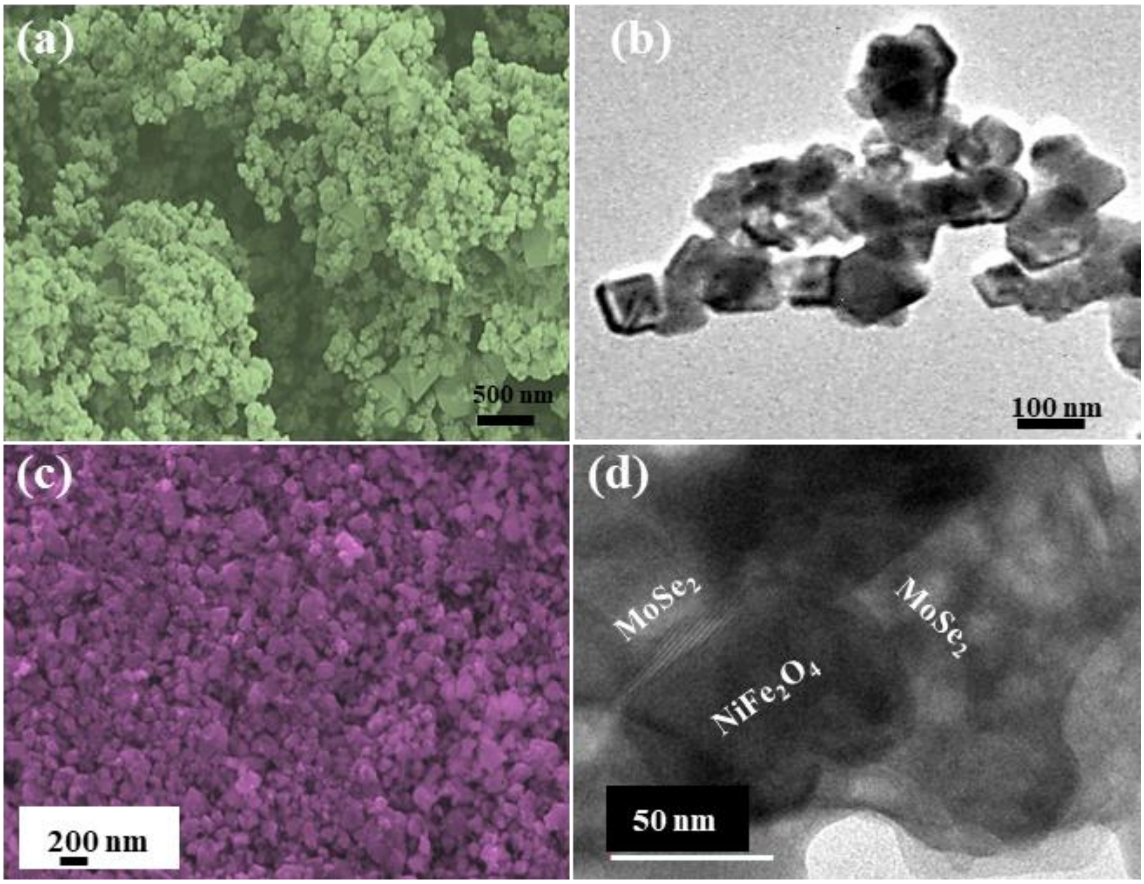

Figure 4.17 (a,c) SEM and (b,d) TEM images for $NiFe_2O_4$ and $NiFe_2O_4$-$MoSe_2$ hybrid nanostructures, respectively.

The XRD analysis is conducted on prepared samples to elucidate their crystallographic structures and phases, as shown in **Figure 4.18 (a)**. The XRD analysis of $NiFe_2O_4$ indicates the presence of characteristic peaks corresponding to the crystallographic planes of cubic spinel $NiFe_2O_4$. Peaks observed at approximately 18.3, 30.1°, 35.4°, 37.1, 43.1°, 53.4°, 56.9°, and 62.5° are attributed to the (111), (220), (311), (222), (400), (422), (511), and (440) planes of $NiFe_2O_4$ (JCPDS no. 00-044-1485) [148, 153, 154]. The XRD analysis of the $NiFe_2O_4$-$MoSe_2$ hybrid nanostructure demonstrates combined peaks corresponding to $NiFe_2O_4$ and $MoSe_2$ phases. Peaks of $MoSe_2$ are observed at approximately 14.0°, 33.5°, and 55.3°, indicative of its (002), (100), and (110) planes, respectively. These peaks affirm the successful synthesis of the $NiFe_2O_4$-$MoSe_2$ hybrid nanostructure. Both prepared materials show the additional peak around ~44.7° (110), which represents the zero-valent iron (Fe) nanoparticle (JCPDS no. 00-006-0696) [149]. Raman spectra of prepared samples are shown in **Figure 4.18 (b)**, exhibiting four clear peaks (T_{2g} (1), E_g, T_{2g} (2) and A_{1g}) corresponding to $NiFe_2O_4$. The A_{1g} mode corresponds to the symmetric stretching of oxygen atoms along the bonds between Fe-O and Ni-O in the tetrahedral sites. The E_g mode is associated with the symmetric bending of oxygen with respect to metal ion. The T_{2g} (2) mode is caused by the asymmetric stretching of Fe (Ni) and O. Lastly, the T_{2g} (1) mode is due to the translational movement of the tetrahedron, which includes the metal ion at the tetrahedral site along with four oxygen atoms [150, 151]. The A_{1g} (~237 cm^{-1}) and E^1_{2g} (~281 cm^{-1}) modes are observed in hybrid nanostructures, belonging to the out-of-plane and in-plane vibrations of $MoSe_2$ [148, 152, 153]. The changes in intensities and Raman shifts for different vibrational modes in $NiFe_2O_4$-$MoSe_2$ hybrid nanostructure compared to pristine $NiFe_2O_4$ es can be attributed to the strong interaction between $NiFe_2O_4$ and $MoSe_2$, indicating the formation of hybrid nanostructure. FTIR spectra, shown in **Figure 4.18 (c)**, indicate the presence of different functional groups in pristine $NiFe_2O_4$ and $NiFe_2O_4$-$MoSe_2$ hybrid nanostructures. FTIR spectrum of $NiFe_2O_4$ shows peak at 458 cm^{-1} associated with tensile vibrations of metal oxide. FTIR spectrum of $NiFe_2O_4$-$MoSe_2$ hybrid nanostructures shows peaks around 844 and 1574 cm^{-1}, corresponding to O-Mo-O and Mo-Se bonds of $MoSe_2$, while the peak at 456 cm^{-1} belongs to metal oxide vibration of $NiFe_2O_4$. Peaks around 3446 cm^{-1} correspond to O-H stretching [74, 113]. The hybrid nanostructure clearly shows the vibrational modes belonging to $MoSe_2$ and $NiFe_2O_4$ with some degree of peak shifting compared to $NiFe_2O_4$, indicating good interaction between them in the hybrid nanostructure.

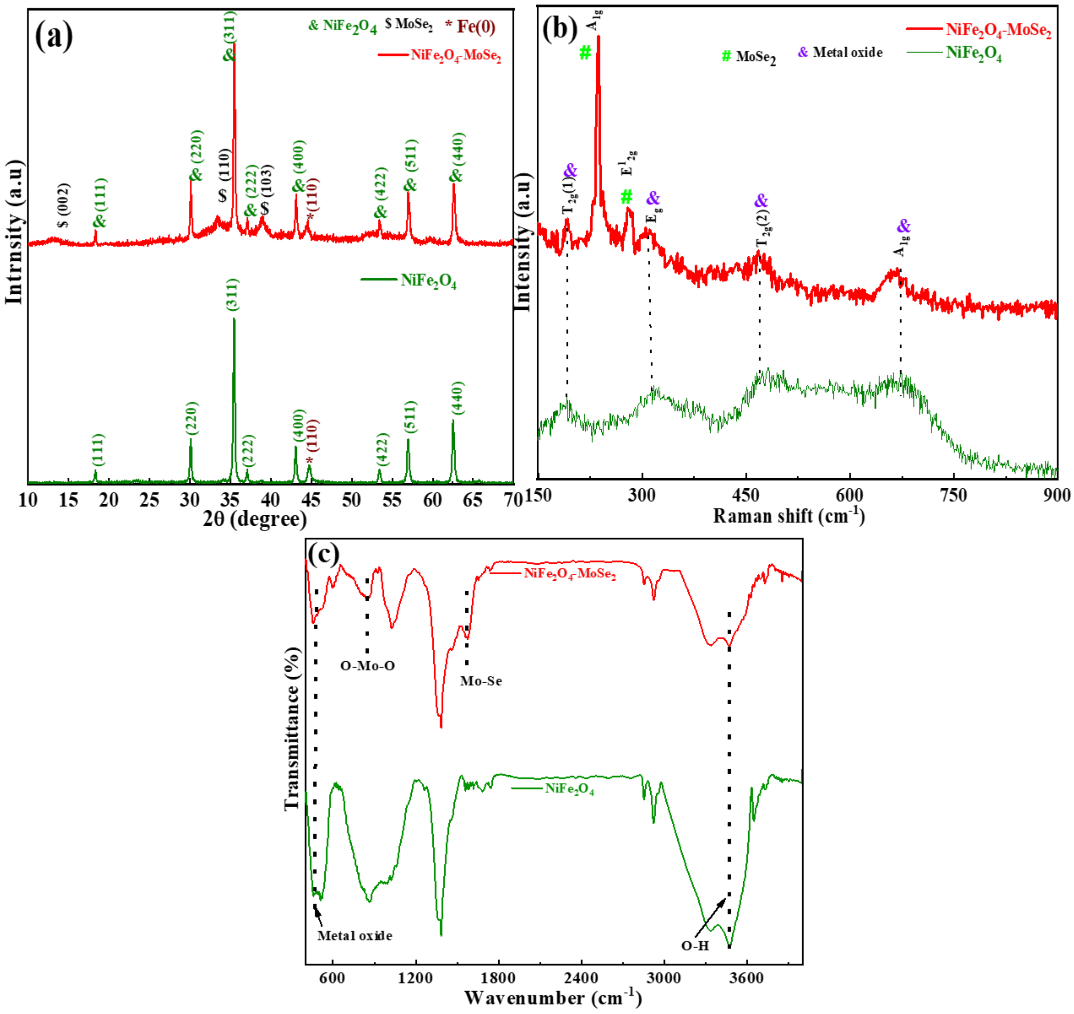

__Figure 4.18__ (a) XRD patterns, (b) Raman and (c) FTIR spectra of $NiFe_2O_4$ and $NiFe_2O_4$-$MoSe_2$ hybrid nanostructure.

The XPS survey spectrum of $NiFe_2O_4$-$MoSe_2$ hybrid nanostructure reveals the presence of Ni 2p, Fe 2p, Mo 3d, Se 3d and O 1s states, as shown in **Figure 4.19 (a)**. The Ni 2p spectrum (**Figure 4.19 (b)**) displays two spin-orbit doublets and two satellite peaks. The Ni $2p_{3/2}$ deconvolutes into two binding energies of ~855.6 eV (Ni^{3+}) and ~857 eV (Ni^{2+}), while Ni $2p_{1/2}$ splits into ~873.2 eV (Ni^{3+}) and ~874.7 eV (Ni^{2+}). The Fe 2p spectrum (**Figure 4.19 (c)**) shows four distinctive peaks centered at ~710.7 eV (Fe^{3+} $2p_{3/2}$), ~713.3 eV (Fe^{2+} $2p_{3/2}$), ~724.6 eV (Fe^{3+} $2p_{1/2}$), and ~727.4 eV (Fe^{2+} $2p_{1/2}$) for $NiFe_2O_4$-$MoSe_2$ hybrid nanostructure.

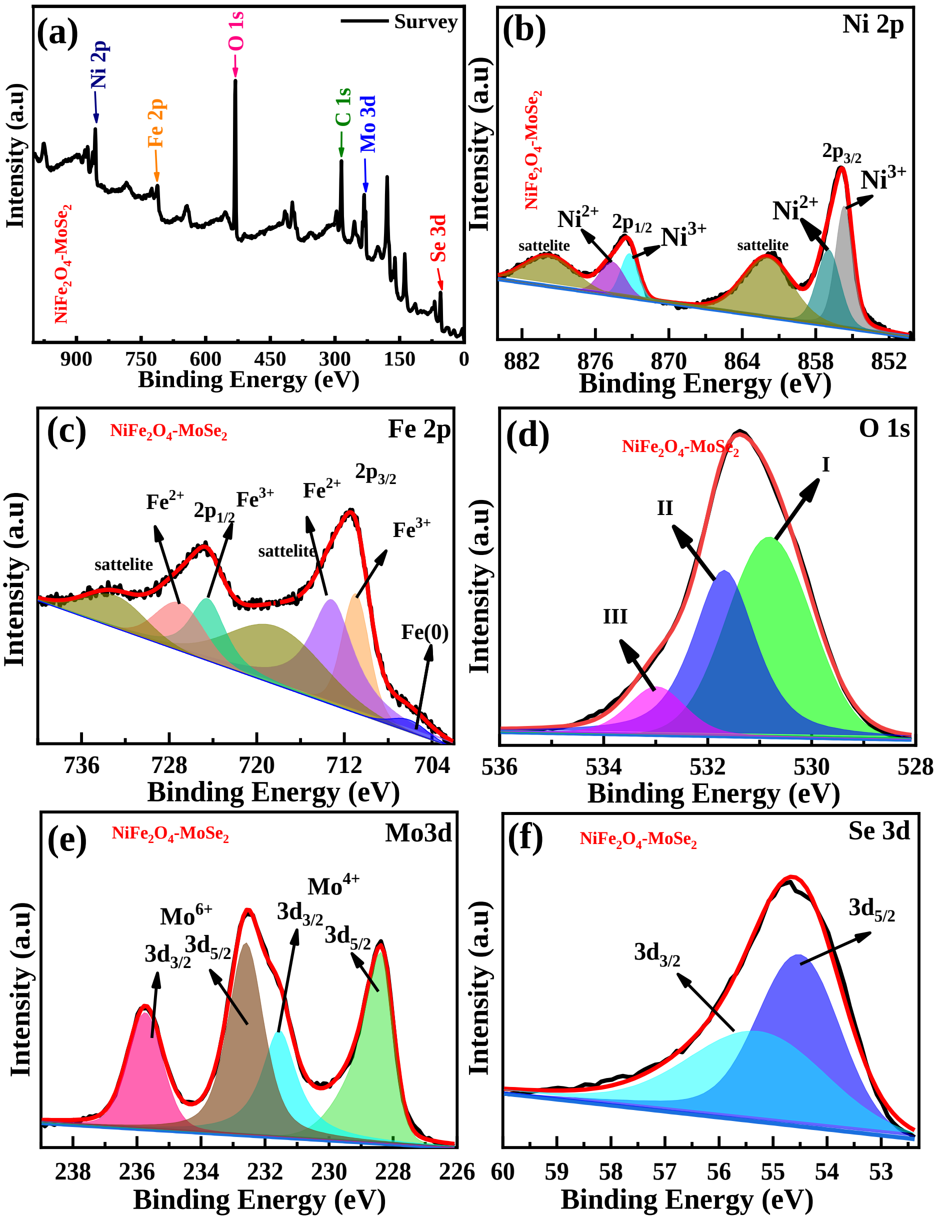

Figure 4.19 *XPS spectra for $NiFe_2O_4$-$MoSe_2$ hybrid nanostructure (a) survey spectrum, spectra for (b) Ni 2p, (c) Fe 2p, (d) O 1s, (e) Mo 3d and (f) Se 3d.*

A very low intense peak at ~705.5 eV confirms the presence of zero-valent iron Fe(0) in $NiFe_2O_4$-$MoSe_2$ hybrid nanostructures. The O 1s spectrum for hybrid nanostructures (**Figure 4.19 (d)**) exhibit three peaks at 530.8 (I), 531.7 (II), and 533 eV (III) for $NiFe_2O_4$-$MoSe_2$, corresponding to metal oxide, defects or low coordination of oxygen ions and chemisorbed oxygen, respectively [148, 154]. The XPS spectrum (**Figure 4.19 (e)**) of Mo3d for $NiFe_2O_4$-$MoSe_2$ show the presence of Mo^{4+} with peaks at ~228.4 eV ($3d_{5/2}$) and ~231.6 eV ($3d_{3/2}$), and Mo^{6+} with peaks at ~232.6 eV ($3d_{5/2}$) and ~235.8 eV ($3d_{3/2}$) due to partial oxidation of Mo [99]. **Figure 4.19 (f)** shows that Se exists in Se^{2-} with peaks at ~54.6 eV for Se $3d_{5/2}$ and ~55.4 eV for Se $3d_{3/2}$ in $NiFe_2O_4$-$MoSe_2$ [81, 129].

4.4.6.2 Electrochemical characterization

OER activity in basic medium

In this study, we have performed LSV measurements for OER activity of prepared electrocatalysts in 1M KOH at a potential sweep rate of 2 mV s^{-1}, as shown in **Figure 4.20 (a)**. The $NiFe_2O_4$-$MoSe_2$ hybrid nanostructure shows a lower overpotential (η_{10}) of 226 mV compared to $NiFe_2O_4$ (η_{10} ~251 mV). The corresponding Tafel slopes (**Figure 4.20 (b)**) of recorded LSV curves show the lower Tafel's slope of 44 mV dec^{-1} for $NiFe_2O_4$-$MoSe_2$ hybrid nanostructure compared to $NiFe_2O_4$ (74 mV dec^{-1}). The high OER electrocatalytic activity of the $NiFe_2O_4$-$MoSe_2$ hybrid nanostructure is primarily attributed to the synergetic effect between $MoSe_2$ and $NiFe_2O_4$. EIS is used to study the electrochemical kinetics of an OER over a range of frequencies (10 mHz to 1 MHz) at a constant overpotential, as shown in **Figure 4.20 (c)**. Nyquist plots of prepared electrocatalysts depict the semicircle-like behavior that is fitted with $R_S(Q_1R_1)(Q_2R_{CT})$ equivalent circuit model, which consists of internal resistance (R_S) due to electrode and electrolyte, resistance (R_1) due to microscopic surface roughness, charge transfer resistance (R_{CT}) as encountered by charge carriers (electrons or ions) and two constant phase elements (Q_1, Q_2) as shown in the inset of **Figure 4.20 (c)**. A lower R_{CT} describes that the electrons can move easily across the electrode-electrolyte interface, allowing for faster and more efficient electron transfer during the OER.

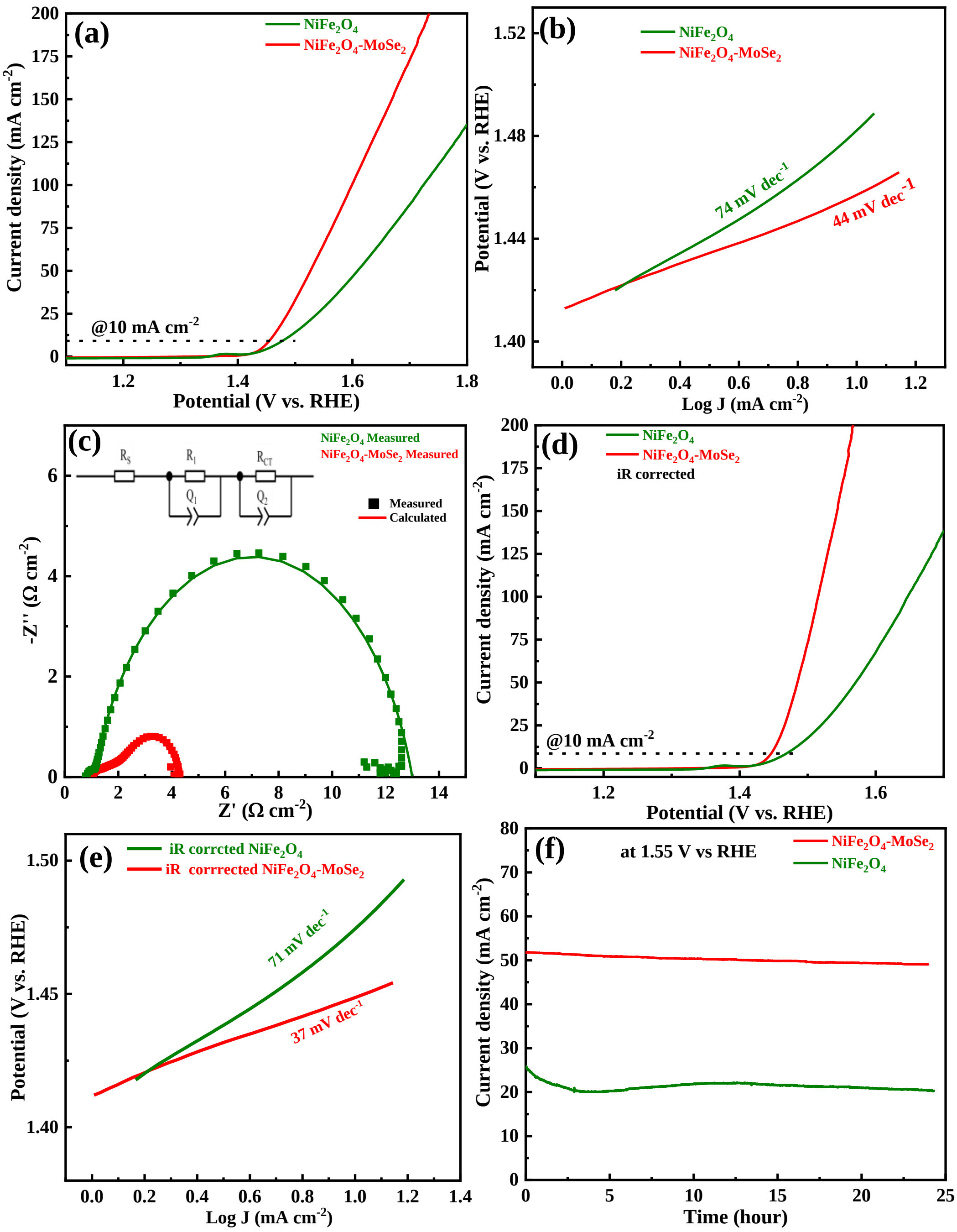

Figure 4.20 *(a) LSV curves, (b) corresponding Tafel plots at potential sweep rates of 2 mV s^{-1}, (c) EIS curves, (d) 90% iR corrected LSV curves (e) corresponding iR corrected Tafel plots and (f) chronoamperometry curves at a constant potential of 1.55 V vs RHE for* $NiFe_2O_4$ *and* $NiFe_2O_4$*-*$MoSe_2$ *hybrid nanostructure in 1M KOH.*

The $NiFe_2O_4$-$MoSe_2$ hybrid nanostructure has the lower R_{CT} value of 1.54 Ω compared $NiFe_2O_4$ (11.5 Ω), again suggesting the better electrocatalytic activity of $NiFe_2O_4$-$MoSe_2$ hybrid nanostructure, as observed in LSV study. The resistance (R_S) of the electrolyte and the electrode-electrolyte interface causes a voltage drop that affects the electrocatalytic performance of the prepared materials. We applied 90% iR correction to compensate this effect**.** This allows us to obtain the true potential and current values for the OER performance. **Figure 4.20 (d)** shows the 90% iR corrected LSV polarization curves at 2 mV s^{-1}, and **Figure 4.20 (e)** shows the corresponding iR corrected Tafel slopes of prepared materials. The $NiFe_2O_4$-$MoSe_2$ hybrid nanostructure shows the lower overpotential (η_{10} ~ 218 mV) and Tafel's slope ~37 mV dec^{-1} compared to $NiFe_2O_4$ (η_{10} ~ 244 mV and Tafel slope~ 71 mV dec^{-1}) after iR correction. In order to examine the stability cum durability of electrocatalysts, we have performed chronoamperometry measurement at a constant potential of 1.55 V vs RHE for 24 hours of continuous operation, as shown in **Figure 4.20 (f)**. We observe that the stability curve of $NiFe_2O_4$-$MoSe_2$ hybrid nanostructure shows a high and stable current density (~94 %), suggesting a high degree of durability compared to $NiFe_2O_4$ (~78%).

In order to calculate ECSA, CV is performed by cycling the potential of a working electrode in a non-faradaic region (1.2 to 1.25 V vs RHE) at different potential sweeps (20, 40, 60, 80, 100 mV s^{-1}) for prepared materials, as shown in **Figure 4.21 (a)** for $NiFe_2O_4$ and **Figure 4.21 (b) for** $NiFe_2O_4$-$MoSe_2$ hybrid nanostructure. Half the average difference of anodic and cathodic current densities is linearly plotted versus potential sweep rates, providing C_{dl} value, as shown in **Figure 4.21 (c)**. The $NiFe_2O_4$-$MoSe_2$ hybrid nanostructure shows the higher C_{dl} value (16.8 mF cm^{-2} or 8.5 mF cm^{-2} mg^{-1}) compared to $NiFe_2O_4$ (7.4 mF cm^{-2} or 4.2 mF cm^{-2} mg^{-1}). The ECSA shows a direct correlation with the C_{dl} and hence a greater C_{dl} value for $NiFe_2O_4$-$MoSe_2$ hybrid nanostructure indicates higher ECSA compared to other prepared electrocatalysts. Further, we have also calculated the number of electrochemically active sites, as described in **equation 4.2-4.3**. The number of active sites (n) are found to be ~1.95×10^{-9} mol mg^{-1} for $NiFe_2O_4$, and ~2.7×10^{-9} mol mg^{-1} for $NiFe_2O_4$-$MoSe_2$ hybrid nanostructure. The hybrid nanostructure shows higher number of active sites compared to pristine $MoSe_2$ (0.76×10^{-9} mol mg^{-1}), as reported in previous section. The reduced agglomeration of nanoparticles and nanosheets in hybrid nanostructures due to probe sonication process provide higher metal active sites and exposed edges of $MoSe_2$ in hybrid nanostructures resulting in higher number of active sites [155-159]. The higher number of electrochemical active sites (*n*) for $NiFe_2O_4$-$MoSe_2$ compared to other prepared electrocatalysts clearly suggests its higher electrocatalytic activity.

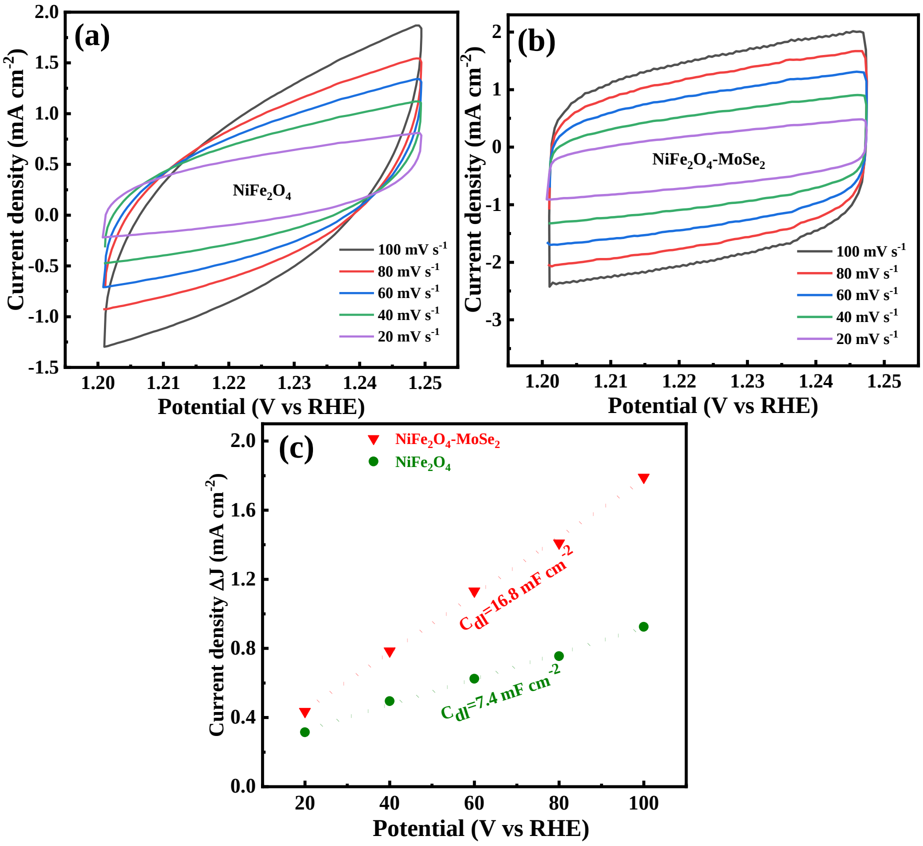

Figure 4.21 *CV curves at different scan rates for (a) $NiFe_2O_4$, (b) $NiFe_2O_4$-$MoSe_2$ hybrid nanostructure and (c) corresponding electrochemical double-layer capacitance (C_{dl}).*

The OER activity of prepared binder-free electrodes ($MoSe_2$-CCP and $MoSe_2$-Ni foam), pristine $MoSe_2$, and Ni decorated over $MoSe_2$ (Ni-$MoSe_2$ (5%), Ni-$MoSe_2$ (10%) and Ni-$MoSe_2$ (20%)), pristine bimetal oxides ($NiCo_2O_4$/NiO, $CoFe_2O_4$, and $NiFe_2O_4$) and hybrid nanostructures ($NiCo_2O_4$/NiO-$MoSe_2$, $CoFe_2O_4$-$MoSe_2$, and $NiFe_2O_4$-$MoSe_2$) have been summarized and compared in **Table 4.1**. Binder-free $MoSe_2$-Ni foam shows better OER performance compared to $MoSe_2$-CCP in 1M KOH. Among Ni-$MoSe_2$ nanocomposites, Ni-

$MoSe_2$ (10%) shows best OER activity, while $NiFe_2O_4$-$MoSe_2$ shows best OER response among hybrid nanostructures.

Table 4.1 The comparative performance summary of OER activity of our studied materials.

Electrocatalysts	**Overpotential (mV)**	**Electrolyte**	**Tafel slope (mV dec^{-1})**	**Ref.**
$MoSe_2$-CCP	296(η_{10}) and 353(η_{50})	1M KOH	36	This work
$MoSe_2$-Ni foam	**292 (η_{50})**	**1M KOH**	**20**	This work
$MoSe_2$	391 (η_{10})	1M KOH	78	This work
Ni-$MoSe_2$ (5%)	306 (η_{10})	1M KOH	66	This work
Ni-$MoSe_2$ (10%)	**277** (η_{10})	**1M KOH**	**53**	This work
Ni-$MoSe_2$ (20%)	293 (η_{10})	1M KOH	57	This work
$CoFe_2O_4$	269 (η_{10})	1M KOH	76	This work
$NiFe_2O_4$	244 (η_{10})	1M KOH	71	This work
$NiCo_2O_4$/NiO	405 (η_{10})	1M KOH	83	This work
$NiCo_2O_4$/NiO-$MoSe_2$	328 (η_{10})	1M KOH	54	This work
$CoFe_2O_4$-$MoSe_2$	226 (η_{10})	1M KOH	61	This work
$NiFe_2O_4$-$MoSe_2$	**218 (η_{10})**	**1M KOH**	**37**	This work
1T/2H$MoSe_2$/MXene	340 (η_{10})	1M KOH	90	[31]
$MoSe_2$/SnS	350 (η_{10})	1M KOH	118	[32]
$MoSe_2$/$Co_{0.85}$Se/NF	229 (η_{10})	1M KOH	48	[124]
RuO_2	275 (η_{10})	1M KOH	49	[126]

4.5 Conclusion

This chapter discuss about performance of binder-free electrodes ($MoSe_2$-CCP and $MoSe_2$-Ni foam) as electrodes, pristine $MoSe_2$, and Ni decorated over $MoSe_2$ (Ni-$MoSe_2$ (5%), Ni-$MoSe_2$ (10%) and Ni-$MoSe_2$ (20%)) nanocomposites, pristine bimetal oxides ($NiCo_2O_4$/NiO, $CoFe_2O_4$, and $NiFe_2O_4$) and hybrid nanostructures ($NiCo_2O_4$/NiO-$MoSe_2$, $CoFe_2O_4$-$MoSe_2$, and $NiFe_2O_4$-$MoSe_2$) as electrocatalyst coated on electrode for OER activity. Binder-free $MoSe_2$-Ni foam shows best OER performance (η_{50} ~292 mV and Tafel' slope ~20 mV dec^{-1}) due to wrinkled vertical structure and presence of 1T and 2H phase, which provides higher number of exposed edges and reduces charge transfer resistance, hence higher active sites for catalytic activity. Amond Ni-$MoSe_2$ nanocomposites, $MoSe_2$-Ni-10 shows lower η_{10} ~277 mV and Tafel slope ~53 mV dec^{-1} compared to Ni-$MoSe_2$ (20%) (η_{10} ~ 293 mV, Tafel slope ~57 mV dec^{-1}), Ni-$MoSe_2$ (5%) (η_{10} ~ 306 mV, Tafel slope ~ 66 mV dec^{-1}), due to due to the optimum presence of Ni atoms over $MoSe_2$, which provides a high synergistic effect between $MoSe_2$ and Ni. Among hybrid nanostructures based materials, $NiFe_2O_4$-$MoSe_2$ shows higher OER activity of (η_{10} ~ 218 mV, Tafel slope ~37 mV dec^{-1}) compared to $CoFe_2O_4$-$MoSe_2$ (η_{10} ~ 226 mV, Tafel slope ~61 mV dec^{-1}) and $NiCo_2O_4$/NiO-$MoSe_2$ (η_{10}~ 328 mV, Tafel's slope ~54 mV $decade^{-1}$). The superior performance of $NiFe_2O_4$-$MoSe_2$ hybrid nanostructures as electrocatalysts for Zn-air batteries is due to the synergistic effect between $MoSe_2$ and $NiFe_2O_4$, which enhances the conductivity, oxygen mobility, and active sites of the catalysts.